symmetry

MDPI

Article

A Mixed Finite Element Approximation for Time-Dependent Navier–Stokes Equations with a General Boundary Condition

Omar El Moutea [1,*], Nadia Nakbi [2], Abdeslam El Akkad [2,3], Ahmed Elkhalfi [3], Lahcen El Ouadefli [3], Sorin Vlase [4,5] and Maria Luminita Scutaru [4,*]

1 Laboratory of Mathematics and Applications-ENS, Hassan II University, Casablanca 20000, Morocco
2 Département de Mathématiques, Centre Regional des Métiers d'Education et de Formation de Fès Meknès (CRMEF Fès-Meknès), Rue de Koweit 49, Ville Nouvelle, Fez 30050, Morocco; nadia.nakbi@usmba.ac.ma (N.N.); abdeslam.elakkad@usmba.ac.ma (A.E.A.)
3 Mechanical Engineering Laboratory, Faculty of Science and Technology, University Sidi Mohammed Ben Abdellah, Route Imouzzer, Fez 30000, Morocco; ahmed.elkhalfi@usmba.ac.ma (A.E.); lahcen.elouadefli@usmba.ac.ma (L.E.O.)
4 Department of Mechanical Engineering, Faculty of Mechanical Engineering, Transylvania University of Brasov, B-dul Eroilor 29, 500036 Brasov, Romania; svlase@unitbv.ro
5 Romanian Academy of Technical Sciences, B-dul Dacia 26, 030167 Bucharest, Romania
* Correspondence: omar.elmoutea-etu@etu.univh2c.ma (O.E.M.); lscutaru@unitbv.ro (M.L.S.)

Abstract: In this paper, we present a numerical scheme for addressing the unsteady asymmetric flows governed by the incompressible Navier–Stokes equations under a general boundary condition. We utilized the Finite Element Method (FEM) for spatial discretization and the fully implicit Euler scheme for time discretization. In addition to the theoretical analysis of the error in our numerical scheme, we introduced two types of a posteriori error indicators: one for time discretization and another for spatial discretization, aimed at effectively controlling the error. We established the equivalence between these estimators and the actual error. Furthermore, we conducted numerical simulations in two dimensions to assess the accuracy and effectiveness of our scheme.

Keywords: a posteriori error indicators; general boundary condition; finite element method (FEM); unsteady incompressible Navier–Stokes equations; IFISS software; COMSOL multiphysics; ADINA system

MSC: 74S05; 76M10; 80M10; 34K10

Citation: El Moutea, O.; Nakbi, N.; El Akkad, A.; Elkhalfi, A.; El Ouadefli, L.; Vlase, S.; Scutaru, M.L. A Mixed Finite Element Approximation for Time-Dependent Navier–Stokes Equations with a General Boundary Condition. *Symmetry* **2023**, *15*, 2031. https://doi.org/10.3390/sym15112031

Academic Editors: Calogero Vetro and Sergei D. Odintsov

Received: 20 September 2023
Revised: 29 October 2023
Accepted: 6 November 2023
Published: 8 November 2023

1. Introduction

The objective of this study is to approach the solution and develop a posteriori error estimations for finite element approximations of the Navier–Stokes equations with a general boundary condition. The Navier–Stokes problem holds significant importance in computational mathematics, particularly for understanding fluid dynamics [1,2]. Specifically, it plays a crucial role in comprehending the intricate behavior of incompressible fluids [3] and finds applications in various domains, including engineering [4], aerodynamics, aeroacoustics [5], and related fields. We will establish the well-posedness of our problem under certain assumptions and rigorously prove the existence and uniqueness of the solution. The Finite Element Method (FEM), a fundamental and widely used numerical technique in engineering and other sciences for modeling and simulating a wide range of problems, served as our primary tool for spatial discretization. In [6], the authors approximated the Navier–Stokes equations with Dirichlet and Neumann boundary conditions using FEM.

Moreover, the authors in this paper [7] employed a conforming FEM to handle time-dependent Navier–Stokes equations, offering valuable insights into the numerical treatment of these nonlinear equations. Several other papers, such as [8–10], explored the application of FEM to address stochastic parabolic problems and the steady Navier–Stokes problem with stabilized techniques, enhancing stability and accuracy. The variational multiscale method, as discussed in [11], was explored as an effective approach to tackle the computational challenges posed by Navier–Stokes equations. Additionally, the mini-element method, presented in [12], is crucial for solving the Navier–Lame equation with a new boundary condition.

A posteriori error estimation is a valuable tool for identifying regions with high approximation errors and guiding adaptive mesh refinement, as discussed in [13]. Quantifying the accuracy of finite element solutions enables adaptive strategies to control errors, effectively balancing computational cost and accuracy in numerical approximations. These strategies optimize computational resources while maintaining accuracy. This technique has been applied to fully discretized time-dependent Stokes equations, as demonstrated in [14]. Effective preconditioning strategies are crucial for achieving fast solutions in nonlinear algebraic systems arising from the problem. This approach quantitatively assesses the accuracy and reliability of numerical solutions. To solve the resulting asymmetry system, we used the Generalized Minimum Residual method (GMRES). In [15], the authors investigated the impact of the discretization order on the preconditioning and convergence of a high-order unstructured Newton-GMRES solver for the Euler equations. Additionally, [16] presented GMRES as a generalized minimal residual algorithm for solving nonsymmetric systems. The literature explores various approaches for defining error estimators based on the residual error estimator, as discussed in [17]. Moreover, in [13], the authors introduced adaptive mesh refinement techniques and multiple error estimators proven equivalent to the energy norm and error.

Our research is focused on developing an approach to solve and analyze the a posteriori error of Navier–Stokes equations with general boundary conditions. We employed the Finite Element Method to approximate the solution and utilized a posteriori error estimation. Specifically, we introduced two types of error indicators “time error indicators”, and “space error indicators”, to assess the accuracy of our numerical solution. This paper’s structure is as follows: In Section 2, we introduce the model problem that forms the foundation of our investigation and define the assumptions necessary for the existence and uniqueness of the solution. Section 3 outlines the discretization approach, utilizing finite elements for approximations, and defines the assumptions to ensure the stability of the scheme. Dedicated to presenting the a posteriori error bounds of the approximated solution and proving the equivalence to the true error, Section 4 is focused on these aspects. Subsequently, in Section 5, we delve into the numerical experiments conducted within the scope of this publication. We provide detailed comparisons with other relevant results to validate the effectiveness of our approach.

2. Time-Dependent Navier–Stokes Equations

This section presents a comprehensive overview of our mathematical model, which revolves around the “time-dependent Navier–Stokes equations” with a general boundary condition. It introduces the model equation and outlines essential assumptions to ensure the problem’s well-posedness, establishing the existence and uniqueness of the solution. Furthermore, it defines the weak formulation of the problem, a crucial step in its mathematical treatment, and sets the foundation for the subsequent analysis and numerical investigations presented in this paper.

We consider a bounded, connected, open domain Ω in $\mathbb{R}^d$ ($d = 2$ or 3), characterized by a Lipschitz continuous connected boundary $\Gamma = \partial\Omega$. The unsteady Navier–Stokes equations are defined by a system of nonlinear partial differential equations, given by

$$\begin{cases} \frac{\partial \vec{u}}{\partial t} - \nu \nabla^2 \vec{u} + \vec{u} \cdot \nabla \vec{u} + \nabla p & = \vec{f} \quad in \quad \mathbb{Q}, \\ \nabla \cdot \vec{u} & = 0 \quad in \quad \mathbb{Q}, \\ \vec{u}(x,0) & = \vec{u}_0(x) \quad in \quad \Omega, \end{cases} \tag{1}$$

where $\mathbb{Q} = \Omega \times [0, T]$ denotes the spatial-temporal domain and $T > 0$ is the final time. The parameter $\nu > 0$ represents the kinematic viscosity, which is a given constant. The unknowns in system (1) are $\overrightarrow{u}$, representing the fluid velocity field, and p, denoting the pressure field, where the operator ∇ denotes the gradient and $\nabla\cdot$ represents the divergence operator.

The general boundary condition is given by

$$C_\beta : \overrightarrow{u} + \beta(x)\,(\nu\nabla\overrightarrow{u} - pI)\overrightarrow{n} = \overrightarrow{g} \text{ in } \Gamma =: \partial\Omega, \tag{2}$$

where $\overrightarrow{n}$ denotes the outward unit normal vector, $\overrightarrow{g}$ belongs to the space $H^{\frac{1}{2}}(\Gamma)$, and $\beta(x)$ is a positive function defined on $\partial\Omega$ that satisfies the following condition: there exist two strictly positive constants, a_1 and b_1, such that

$$a_1 \leq \frac{1}{\beta(x)} \leq b_1, \quad \forall x \in \Gamma. \tag{3}$$

Remark 1. *According to the β values, we can consider:*

- *If $\beta \prec\prec 1$, then C_β represents the Dirichlet boundary condition.*
- *If $\beta \succ\succ 1$, then C_β represents the Neumann boundary condition.*

Now, we define the function spaces used to represent mathematical solutions. The function spaces used in this study are typically denoted as follows:
Space for velocity:

$V = \left(H_0^1(\Omega)\right)^2$, $W = \left(L^2(\Omega)\right)^2$,
$X = \{\overrightarrow{v} \in W : \operatorname{div}\overrightarrow{v} = 0,\ \overrightarrow{v}\cdot\overrightarrow{n}|_{\partial\Omega} = 0\}$,
$Y = \{\overrightarrow{v} \in V : \operatorname{div}\overrightarrow{v} = 0\}$,
$V = \left(H_0^1(\Omega)\right)^2$, $W = \left(L^2(\Omega)\right)^2$.

Space for pressure:

$$Q = \{q \in L^2(\Omega) : \textstyle\int_\Omega q(x)\,dx = 0\}.$$

Let us define the Stokes operator as $A = -P\Delta$, where P represents the L^2-orthogonal projection of W onto X. The domain of A, denoted by $D(A)$, is given by

$$D(A) = \left(H^2(\Omega)\right)^2 \cap Y.$$

Let us consider these assumptions:

(A_1) The domain Ω is a smooth domain.

(A_2) There exists a unique solution $(\overrightarrow{v}, q) \in (V, Q)$ for the Stokes problem that satisfies the inequality $|\overrightarrow{v}|_2 + |q|_1 \leq C|\overrightarrow{g}_1|_0$ for all $\overrightarrow{g}_1 \in W$. The Stokes problem is defined by

$$\begin{cases} -\nu\Delta\overrightarrow{v} + \nabla q & = \overrightarrow{g}_1 \quad \text{in } \Omega, \\ \operatorname{div}\overrightarrow{v} & = 0 \quad \text{in } \Omega, \\ \overrightarrow{v} & = 0 \quad \text{on } \Gamma, \end{cases} \tag{4}$$

where $C > 0$ is a constant that depends on Ω and ν. For more details, we refer to [18].

(A_3) $\overrightarrow{f}(x,t) \in C^0(0, T, W) \cap L^2\big(0, T, H^1(\Omega)\big)$.

(A_4) $\overrightarrow{f}_t(x,t) \in L^2\big(0, T, L^2(\Omega)\big)$.

(A_5) $\overrightarrow{u}_0(x) \in D(A)$.

Under these assumptions, problems (1) and (2) have a unique solution; see [18] for more details.

Let us define the bilinear forms $a : V \times V \to \mathbb{R}$, $b : V \times Q \to \mathbb{R}$ and $d_1 : Q \times Q \to \mathbb{R}$ as follows:

$$\begin{aligned} a(\overrightarrow{u}, \overrightarrow{v}) &= \nu \int_\Omega \nabla \overrightarrow{u} : \nabla \overrightarrow{v}\, dx + \int_\Gamma \frac{1}{\beta} \overrightarrow{u} \cdot \overrightarrow{v} ds, \\ b(\overrightarrow{v}, q) &= \int_\Omega (q, \mathrm{div}, \overrightarrow{v})\, dx, \\ d_1(p, q) &= \int_\Omega pq\, dx, \end{aligned}$$

for all $\overrightarrow{u}, \overrightarrow{v} \in V$. We define the nonlinear form $D : V \to \mathbb{R}$ as follows:

$$D(\overrightarrow{u}, \overrightarrow{v}) = (\overrightarrow{u} \cdot \nabla)\overrightarrow{v} + \frac{1}{2}(\mathrm{div}\ \overrightarrow{u})\overrightarrow{v},$$

and the trilinear form $d : V \times V \times V \to \mathbb{R}$ by

$$\begin{aligned} d(\overrightarrow{u}, \overrightarrow{v}, \overrightarrow{w}) &= \langle D(\overrightarrow{u}, \overrightarrow{v}), \overrightarrow{w} \rangle_{V',V} \\ &= ((\overrightarrow{u} \cdot \nabla)\overrightarrow{v}, \overrightarrow{w}) + \frac{1}{2}((\nabla \cdot \overrightarrow{u})\overrightarrow{v}, \overrightarrow{w}) \\ &= \frac{1}{2}((\overrightarrow{u} \cdot \nabla)\overrightarrow{v}, \overrightarrow{w}) - \frac{1}{2}((\overrightarrow{u} \cdot \nabla)\overrightarrow{w}\ \overrightarrow{v}), \end{aligned}$$

for all $\overrightarrow{u}, \overrightarrow{v}, \overrightarrow{w} \in V$. The continuous linear functional $l : V \to \mathbb{R}$ is defined as follows:

$$l(\overrightarrow{v}) = \int_\Omega \overrightarrow{f} \cdot \overrightarrow{v}\, dx + \int_\Gamma \frac{1}{\beta} \overrightarrow{g} \cdot \overrightarrow{v}\, dx. \tag{5}$$

These inner products induce norms on V and Q, denoted by $\|\cdot\|_V$ and $\|\cdot\|_Q$, which are defined as follows:

$$\|\overrightarrow{v}\|_V = a(\overrightarrow{v}, \overrightarrow{v})^{\frac{1}{2}}, \qquad \|q\|_Q = d_1(q, q)^{\frac{1}{2}}, \tag{6}$$

for all $\overrightarrow{u} \in V$, $q \in Q$, and we define this norm as follows:

$$[\overrightarrow{v}](t) = \left(\|\overrightarrow{v}(\cdot, t)\|^2_{L^2(\Omega)^2} + \nu \int_0^t \|\nabla \overrightarrow{v}(\cdot, s)\|^2_{L^2(\Omega)} ds \right)^{\frac{1}{2}}. \tag{7}$$

For more detailed information and properties regarding this norm, see [14,19]. These references offer further insights and analysis related to the norm $[\cdot](t)$ within the presented framework. Now, let us state the weak formulation of the unsteady Navier–Stokes problems (1) and (2) as follows. Find $(\overrightarrow{u}, p) \in V \times Q$, such that

$$\left\{ \begin{array}{ll} \overrightarrow{u}(\cdot, 0) = \overrightarrow{u}_0 \quad in\ \Omega, & \\ (\frac{\partial \overrightarrow{u}}{\partial t}, \overrightarrow{v}) + a(\overrightarrow{u}, \overrightarrow{v}) - b(\overrightarrow{v}, p) + d(\overrightarrow{u}, \overrightarrow{u}, \overrightarrow{v}) & = l(\overrightarrow{v}), \\ -b(\overrightarrow{u}, q) & = 0, \end{array} \right. \tag{8}$$

for all $(\overrightarrow{v}, q) \in V \times Q$ and $t \in (0, T)$. We consider the functions β and $\overrightarrow{g}$ in (2) to be equal to zero in a small part of the boundary. This condition is necessary to ensure the uniqueness of the solution.

The existence and uniqueness of the solution of the weak formulation (8) under the assumptions (A_1)–(A_5) have been proven in various papers; see, for example, Ref. [18].

3. Finite Element Approximation

The finite element approximation provides a powerful and flexible approach to address the nonlinearities and complexities present in the governing equations, making it well-suited for our purposes. Our focus is to approximate the solution of the governing

Equations (1) and (2). To achieve this, we utilize the Finite Element Method (FEM) in the spatial domain, benefiting from its versatility and robustness in handling complex geometries and boundary conditions. Furthermore, we adopt the fully-implicit Euler method in the time domain, as it efficiently and accurately captures the time-dependent behavior of the fluid flow. By combining the spatial discretization through FEM and the time integration using the fully-implicit Euler method, we establish a comprehensive numerical framework for approximating the solution.

Let τ_h with $h > 0$ be a family of triangulations of the domain Ω. In this context, we define h_K as the diameter of a simplex K and h_E as the diameter of a face E. The parameter h is then defined as the maximum of h_K over all $K \in \tau_h$ ($h = \max_{K\in\tau_h}\{h_K\}$). For each $K \in \tau_h$, we denote the set of edges (respectively, vertices) of K as $\varepsilon(K)$ (respectively, $N(K)$). Additionally, we introduce the set ε_h, which consists of all edges split into interior and boundary edges. Specifically, we have $\varepsilon_h = \varepsilon_{h,\Omega} \cup \varepsilon_{h,\Gamma}$, where $\varepsilon_{h,\Omega}$ denotes the set of edges in the interior of Ω, and $\varepsilon_{h,\Gamma}$ denotes the set of edges on the boundary $\partial\Omega$.

For the time discretization, we divide the interval $[0, T]$ into subintervals $[t_{n-1}, t_n]$, with corresponding time steps $\Delta t_n = t_n - t_{n-1}$ for $n = 1, 2, \cdots, N$. Here, $0 = t_0 < t_1 < \cdots < t_N = T$, and $\tau = (\tau_1, \tau_2, \cdots, \tau_N)$ denotes the N-tuple of time steps. The regularity parameter δ_τ is defined as the maximum ratio of time steps between consecutive intervals, given by $\delta_\tau = \max_{2\le n\le N} \frac{\Delta t_n}{\Delta t_{n-1}}$. This parameter provides a measure of the irregularity or variation in the time step sizes throughout the discretization process.

We define the function $\overrightarrow{v}\tau$ on the interval $[0, T]$, which is affine on each subinterval $[t_{n-1}, t_n]$ for $1 \le n \le N$ as follows:

$$\overrightarrow{v}\tau = \frac{t - t_{n-1}}{\Delta t_n}\overrightarrow{v}^n + \frac{t_n - t}{\Delta t_n}\overrightarrow{v}^{n-1}. \tag{9}$$

In (9), $\overrightarrow{v}^n$ (respect $\overrightarrow{v}^{n-1}$) represents the values of the velocity field at time instances t_n (respect t_{n-1}).

For any Banach space F, we define $W_\tau(F)$ as the space of functions $\overrightarrow{v}\tau$ defined on the interval $[0, T]$ and obtained from the family $(\overrightarrow{v}^n)_{0\le n\le N} \in F^{N+1}$. The discrete norm on the space $W_\tau\big(H_0^1(\Omega)\big)$ is defined by

$$[[\overrightarrow{v}_\tau]](t_n) = \left(\|\overrightarrow{v}^n\|^2_{L^2(\Omega)^2} + \nu\sum_{m=1}^{n}\Delta t_m\|\nabla\overrightarrow{v}^m\|^2_{L^2(\Omega)}\right)^{\frac{1}{2}}, \tag{10}$$

for all $n = 1, \cdots, N$.

The finite element approximation to (1) and (2) is as follows. Find the vector $(\overrightarrow{u}^n)_{0\le n\le N} \in W \times V^N$ and $(p^n)_{1\le n\le N} \in Q^N$, such that

$$\left\{\begin{array}{lcl} \overrightarrow{u}^0 = \overrightarrow{u}_0 \text{ in } \Omega, & & \\ \frac{1}{\Delta t_n}(\overrightarrow{u}^n - \overrightarrow{u}^{n-1}, \overrightarrow{v}) + a(\overrightarrow{u}^n, \overrightarrow{v}) - b(\overrightarrow{v}, p^n) + d(\overrightarrow{u}^n, \overrightarrow{u}^n, \overrightarrow{v}) & = & (\overrightarrow{f}^n, \overrightarrow{v}) + \frac{1}{\beta}(\overrightarrow{g}^n\cdot\overrightarrow{v})_\Gamma, \\ -b(\overrightarrow{u}^n, q) & = & 0, \end{array}\right. \tag{11}$$

for all $(\overrightarrow{v}, q) \in V \times Q$.

Let V_h and Q_h be the approximation spaces for the $Q_1 - P_0$ approximation. We employ the stabilized $Q_1 - P_0$ method and a trapezoidal rule time stepping scheme; see [20] for more details. The goal is to find the pair $(\overrightarrow{d}_h^{n+1}, p_h^{n+1}) \in V_h \times Q_h$, such that

$$\left\{\begin{array}{lcl} 2(\overrightarrow{d}_h^{n+1}, \overrightarrow{v}_h) + \nu\Delta t_{n+1}(\nabla\overrightarrow{d}_h^{n+1}, \nabla\overrightarrow{v}_h) & + & \Delta t_{n+1}(\overrightarrow{w}_h^{n+1}\cdot\nabla\overrightarrow{d}_h^{n+1}, \overrightarrow{v}_h) - (p_h^{n+1}, \nabla\cdot\overrightarrow{v}_h) \\ & = & (\frac{\partial\overrightarrow{u}_h^n}{\partial t}, \overrightarrow{v}_h) - \nu(\nabla\overrightarrow{u}_h^n, \nabla\overrightarrow{v}_h) - (\overrightarrow{w}_h^{n+1}\cdot\nabla\overrightarrow{u}_h^n, \overrightarrow{v}_h), \\ -(\nabla\cdot\overrightarrow{d}_h^{n+1}, q_h) - \alpha\,\gamma(p_h^{n+1}, q_h) & = & 0, \end{array}\right.$$

for all $(\overrightarrow{v}_h, q_h) \in V_h \times Q_h$, where

$$\overrightarrow{w}_h^{n+1} = (1 + \frac{\Delta t_{n+1}}{\Delta t_n})\overrightarrow{u}_h^n - \frac{\Delta t_{n+1}}{\Delta t_n}\overrightarrow{u}_h^{n-1}.$$

The velocity vectors are approached by

$$\overrightarrow{u}_h^{n+1} = \overrightarrow{u}_h^n + \Delta t_{n+1}\overrightarrow{d}_h^n,$$

and acceleration at t_{n+1} is defined by

$$\frac{\partial \overrightarrow{u}_h^{n+1}}{\partial t} = 2\overrightarrow{d}_h^n - \frac{\partial \overrightarrow{u}_h^n}{\partial t}.$$

The stabilization parameter $\gamma_K(p_h, q_h)$ is defined as follows:

$$\gamma_K(p_h, q_h) := \frac{|K|}{4}\sum_{E\in\Gamma_K}\frac{1}{h_E}\int_E [[p_h]]_E[[q_h]]_E,$$

and the stabilization term $\gamma(p_h, q_h)$ is defined as follows:

$$\gamma(p_h, q_h) := \sum_{K\in T_K}\gamma_K(p_h, q_h),$$

where Γ_K is the set consisting of the four interior element edges in the macroelement K, T_K is a macroelement partitioning of the domain Ω, $|K|$ is the mean element area within the macroelement, $[[\cdot]]_E$ is the jump across edge E, and h_E is the length of E.

Stabilized terms are introduced in the numerical scheme to ensure its stability and demonstrate the existence of a solution. For more detailed information, refer to [21,22]. We assume the necessary assumptions to ensure the stability of the scheme.

(A_6) Let the space $X^1_{n,h}$ be defined by

$$X^1_{n,h} = \{\overrightarrow{v}_n \in V : \forall K \in \tau_{n,h}, \overrightarrow{v}_h|_K \in P_2(K)\}, \tag{12}$$

such that

$$X^1_{n,h} \subset V_{n,h},$$

where $P_2(K)$ is the space of polynomials of degree ≤ 2, for all $K \in \tau_{n,h}$.

(A_7) For $1 \leq n \leq N$, there exists a constant $\gamma_{n,h} > 0$, such that

$$\sup_{\overrightarrow{v}_h \in V_{n,h}} \frac{(\nabla\cdot\overrightarrow{v}_h, q_h)}{\|\nabla\overrightarrow{v}_h\|_{L^2(\Omega)}} \geq \gamma_{n,h}\|q_h\|_{L^2(\Omega)}, \tag{13}$$

for all $q_h \in Q_{n,h}$.

Under these assumptions (A_1)–(A_7), there exists a solution for the approximated problem. Please refer to [23,24] for more details. We define the following space:

$$Y_{n,h} = \{\overrightarrow{v}_n \in V_{n,h}; (\nabla\cdot\overrightarrow{v}_h, q_h) = 0, \forall q_h \in Q_{n,h}\}. \tag{14}$$

Let π_h be the projection operator from $L^2(\Omega)$ onto $V_{0,h}$. We initialize the approximate velocity field $\overrightarrow{u}_h^0 \in V_{0,h}$, as well as the pressure field $p_h^0 = 0$. We find $(\overrightarrow{u}_h^n)_{0\leq n\leq N} \in \prod_{n=0}^N V_{n,h}$ and $(p_h^n)_{1\leq n\leq N} \in \prod_{n=0}^N Q_{n,h}$, such that

$$\begin{cases} \overrightarrow{u}_h^0 = \pi_h\overrightarrow{u}_0 \text{ in } \Omega, & \\ \frac{1}{\Delta t_n}(\overrightarrow{u}_h^n - \overrightarrow{u}_h^{n-1}, \overrightarrow{v}_h) + d(\overrightarrow{u}_h^n, \overrightarrow{u}_h^n, \overrightarrow{v}_h) - b(\overrightarrow{v}_h, p_h^n) + a(\overrightarrow{u}_h^n, \overrightarrow{v}_h) &= (\overrightarrow{f}^n, \overrightarrow{v}_h) + \frac{1}{\beta}(\overrightarrow{g}^n\cdot\overrightarrow{v}_h)_\Gamma, \\ -b(\overrightarrow{u}_h^n, q_h) &= 0, \end{cases} \tag{15}$$

for all $(\overrightarrow{v}_h, q_h) \in V_{n,h} \times Q_{n,h}$ and $1 \leq n \leq N$.

We use a set of vector-valued basis functions $\{\overrightarrow{\varphi_i}\}_{i=1,\cdots,n_u}$ so that

$$\overrightarrow{u}_h = \sum_{i=1}^{n_u} u_i \overrightarrow{\varphi_i}. \tag{16}$$

We introduce a set of pressure basis functions $\{\psi_k\}_{k=1,\cdots,n_p}$ so that

$$p_h = \sum_{k=1}^{n_p} p_k \psi_k, \tag{17}$$

where, n_u and n_p represent the numbers of velocity and pressure basis functions, respectively. This leads to a nonlinear system of algebraic equations defined as follows:

$$\begin{cases} D\frac{dU}{dt}(t) + [N(U(t)) + M]U(t) + BP(t) & = L(t), \\ B^T U(t) & = 0. \end{cases} \tag{18}$$

The vertices of the unknowns are defined by

$$U(t) = (u_1(t), u_2(t), \cdots, u_{n_u}(t))^T, \tag{19}$$

$$P(t) = (p_1(t), p_2(t), \cdots, p_{n_p}(t))^T. \tag{20}$$

The matrix B is the divergence matrix defined by

$B = [b_{k,j}]$, where $b_{k,j} = -\int_\Omega \psi_k \nabla \cdot \overrightarrow{\varphi}_j$,

and

$D = [d_{ij}]$, where $d_{ij} = \int_\Omega \overrightarrow{\varphi}_i \cdot \overrightarrow{\varphi}_j$,

$N = [n_{ij}]$, where $n_{ij} = \sum_{k=1}^{n_u} u_k(t) \int_\Omega (\overrightarrow{\varphi}_j \cdot \nabla \overrightarrow{\varphi}_k) \cdot \overrightarrow{\varphi}_i$,

$M = [m_{ij}]$, where $m_{ij} = \nu \int_\Omega \nabla \overrightarrow{\varphi}_i : \nabla \overrightarrow{\varphi}_j + \int_{\partial\Omega} \frac{1}{\beta} \overrightarrow{\varphi}_i \cdot \overrightarrow{\varphi}_j$,

$L = [l_i]$, where $l_i = \int_\Omega \overrightarrow{f} \cdot \overrightarrow{\varphi}_i + \int_{\partial\Omega} \frac{1}{\beta} \overrightarrow{g} \cdot \overrightarrow{\varphi}_i$,

for $i, j = 1, \cdots, n_u$, $k = 1, \cdots, n_p$.

The solution of the nonlinear system (1) and (2) can be efficiently carried out using Picard's method. Within each iteration of Picard's method, we need to solve a linear system with the following generic form:

$$\begin{pmatrix} A_0 + N & B_0^T \\ B_0 & 0 \end{pmatrix} \begin{pmatrix} U \\ P \end{pmatrix} = \begin{pmatrix} L \\ 0 \end{pmatrix}. \tag{21}$$

To accelerate the solution of the nonsymmetric system (21) arising from the Picard iterations, we employ the Generalized Minimum Residual method (GMRES), see [16], (GMRES is an iterative method designed for solving general systems. It provides a flexible and robust approach to handle nonsymmetric matrices). For more detailed information about the GMRES method and the specific preconditioning techniques employed in this context, you can refer to the cited references [16,24–26]. They provide further insights into the theoretical background and practical implementation of these methods for solving nonlinear equations. This preconditioner is known to be effective in improving the convergence of iterative methods for solving the Navier–Stokes equations.

4. Error Estimates

In the remaining part of this paper, we restrict our analysis to the case where the spatial dimension is limited to two dimensions.

In this section, our attention is directed toward defining the a posteriori error estimation for our problem. We introduce two types of error indicators to assess the accuracy of our solution: time error indicators and space error indicators. These indicators enable us to quantify the errors present in both the temporal and spatial domains, providing valuable insights into the quality of our numerical approximation. We establish upper bounds for the error estimators to further analyze and characterize the errors. These bounds give us an estimate of the maximum potential error in our solution. Moreover, we establish the equivalence between these error indicators and the error, affirming that our error estimators offer reliable approximations of the overall error in the solution.

Let $\overrightarrow{f}_h^n$ be the approximation of $\overrightarrow{f}^n$, which is a polynomial of degree $\leq l$ on all elements of $\tau_{n,h}$. Here, $[\cdot]_E$ represents the jump across the edge E in the direction of the outward unit normal vector $\overrightarrow{n}_E$ for each $E \in \varepsilon(K)$.

We define the time error indicator as follows:

$$\eta^n = \sqrt{\frac{\Delta t_n}{3}\nu}\|\nabla(\overrightarrow{u}_h^n - \overrightarrow{u}_h^{n-1})\|_{L^2(\Omega)}, \qquad 1 \leq n \leq N, \tag{22}$$

and the space error indicator by

$$\begin{aligned} \eta_K^n &= h_K\|\overrightarrow{f}_h^n - \frac{\overrightarrow{u}_h^n - \overrightarrow{u}_h^{n-1}}{\Delta t_n} + \nu\Delta\overrightarrow{u}_h^n - \nabla p_h^n - (\overrightarrow{u}_h^n \cdot \nabla)\overrightarrow{u}_h^n\|_{L^2(K)} \\ &\quad + \sum_{E\in\varepsilon(K)} h_E^{\frac{1}{2}}\|[\nu\partial_{n_E}\overrightarrow{u}_h^n - p_h^n\overrightarrow{n}_E]_E\|_{L^2(E)} + \nu\|\mathrm{div}\,\overrightarrow{u}_h^n\|_{L^2(K)}. \end{aligned} \tag{23}$$

The time error indicators η^n are local in time and global in space, while the space error indicators η_K^n are local in both time and space.

Theorem 1. *Under the assumptions (A_1)–(A_7), problem (8) has a unique solution denoted by $\overrightarrow{u} \in L^p(0,t;X) \cap L^2(0,t;Y)$. This solution satisfies*

$$\|\overrightarrow{u}(t)\|_0^2 + \|\nabla\overrightarrow{u}(t)\|_0^2 + \|A\overrightarrow{u}(t)\|_0^2 + \|\nabla p(t)\|_0^2 + \|\overrightarrow{u}_t(t)\|_0^2 \leq K_1, \tag{24}$$

$$\int_0^t \{\|\nabla\overrightarrow{u}\|_0^2 + \|\overrightarrow{u}_t\|_0^2 + \|A\overrightarrow{u}\|_0^2 + \|\nabla p\|_0^2 + \|\nabla\overrightarrow{u}_t\|_0^2\}ds \leq K_1, \tag{25}$$

where K_1 is a positive constant, and we have

$$\begin{aligned} [\overrightarrow{u}](t) &\leq \left(\tfrac{1}{\nu}\|\overrightarrow{f}\|^2_{L^2(0,t;H^{-1}(\Omega)^2)} + \|\overrightarrow{u}_0\|^2_{L^2(\Omega)}\right)^{\frac{1}{2}}, \\ \|\tfrac{\partial\overrightarrow{u}}{\partial t} + (\overrightarrow{u}\cdot\nabla)\overrightarrow{u} + \nabla p\|_{L^2\left(0,t;H^{-1}(\Omega)^2\right)} &\leq 2\left(\|\overrightarrow{f}\|^2_{L^2(0,t;H^{-1}(\Omega)^2)} + \tfrac{\nu}{2}\|\overrightarrow{u}_0\|^2_{L^2(\Omega)}\right)^{\frac{1}{2}}. \end{aligned} \tag{26}$$

Proof. Readers can refer to the paper in [9] for these results. □

For all $t \in [t_{n-1}, t_n]$, where $n = 1, \cdots, N$, we define the following equation:

$$\overrightarrow{v}_{h\tau} = \frac{t - t_{n-1}}{\Delta t_n}\overrightarrow{v}_h^n + \frac{t_n - t}{\Delta t_n}\overrightarrow{v}_h^{n-1}. \tag{27}$$

We will use these notations throughout the rest of the document: $\overrightarrow{u}$ is a solution to the problem (8), $\overrightarrow{u}_\tau$ is the solution of (11), and $\Pi_\tau\overrightarrow{f}$ is the step function, which is constant and equal to $\overrightarrow{f}(t_n)$ on each interval $[t_{n-1}; t_n]$ for all $n = 1, \cdots, N$.

Theorem 2. *Under the assumptions (A_1)–(A_7), the following estimates are valid:*

$$[\overrightarrow{u} - \overrightarrow{u}_\tau](t_n) \leq \beta_1\left(\sum_{m=1}^{n}\frac{1}{\nu}(\eta^m)^2 + \|\overrightarrow{u}_\tau - \overrightarrow{u}_{h\tau}\|^2_{L^2(0,t_n;H^1(\Omega))} + \frac{1}{\nu}\|\overrightarrow{f} - \Pi_\tau\overrightarrow{f}\|^2_{L^2(0,t_n;H^{-1}(\Omega))}\right)^{\frac{1}{2}}, \tag{28}$$

for all $n = 1, \cdots, N$, where β_1 is a positive constant that depends on ν and $\overrightarrow{f}$.

Proof. By using the solutions of systems (8) and (11), we have

$$(\overrightarrow{u} - \overrightarrow{u}_\tau)(\cdot, 0) = 0 \text{ in } \Omega, \tag{29}$$

and we have

$$\begin{aligned}
\left(\frac{\partial}{\partial t}(\overrightarrow{u} - \overrightarrow{u}_\tau), \overrightarrow{v}\right) \quad &+ \quad a(\overrightarrow{u} - \overrightarrow{u}_\tau, \overrightarrow{v}) - b(\overrightarrow{v}, p - \Pi_\tau p_\tau) + d(\overrightarrow{u}, \overrightarrow{u}, \overrightarrow{v}) - d(\overrightarrow{u}_\tau, \overrightarrow{u}_\tau, \overrightarrow{v}) \\
&= \quad (\overrightarrow{f} - \Pi_\tau \overrightarrow{f}, \overrightarrow{v}) + a(\overrightarrow{u}^n - \overrightarrow{u}_\tau, \overrightarrow{v}) + d(\overrightarrow{u}^n, \overrightarrow{u}^n, \overrightarrow{v}) - d(\overrightarrow{u}_\tau, \overrightarrow{u}_\tau, \overrightarrow{v}), \qquad (30) \\
-b(\overrightarrow{u} - \overrightarrow{u}_\tau, q) \quad &= \quad 0, \qquad (31)
\end{aligned}$$

for all $(\overrightarrow{v}, q) \in V \times Q$.
Therefore, employing $(\overrightarrow{v}, q) = (\overrightarrow{u} - \overrightarrow{u}_\tau, p - \Pi_\tau p_\tau)$ in (30), we infer

$$\begin{aligned}
&\frac{1}{2}\frac{d}{dt}\|\overrightarrow{u} - \overrightarrow{u}_\tau\|^2_{L^2(\Omega)} + \nu\|\nabla(\overrightarrow{u} - \overrightarrow{u}_\tau)\|^2_{L^2(\Omega)} + d(\overrightarrow{u}, \overrightarrow{u}, \overrightarrow{u} - \overrightarrow{u}_\tau) - d(\overrightarrow{u}_\tau, \overrightarrow{u}_\tau, \overrightarrow{u} - \overrightarrow{u}_\tau) = \\
&(\overrightarrow{f} - \Pi_\tau \overrightarrow{f}, \overrightarrow{u} - \overrightarrow{u}_\tau) + a(\overrightarrow{u}^n - \overrightarrow{u}_\tau, \overrightarrow{u} - \overrightarrow{u}_\tau) + d(\overrightarrow{u}^n, \overrightarrow{u}^n, \overrightarrow{u} - \overrightarrow{u}_\tau) - d(\overrightarrow{u}_\tau, \overrightarrow{u}_\tau, \overrightarrow{u} - \overrightarrow{u}_\tau).
\end{aligned}$$

By employing the bound of $d(\overrightarrow{u}, \overrightarrow{v}, \overrightarrow{w})$ and utilizing function space (14), along with the first equation of problem (15), and inequalities (24)–(26), we can deduce the following inequalities:

$$d(\overrightarrow{u}^n, \overrightarrow{u}^n, \overrightarrow{u} - \overrightarrow{u}_\tau) - d(\overrightarrow{u}_\tau, \overrightarrow{u}_\tau, \overrightarrow{u} - \overrightarrow{u}_\tau) \le \beta_2|\overrightarrow{u}^n - \overrightarrow{u}_\tau|_1|\overrightarrow{u} - \overrightarrow{u}_\tau|_1, \tag{32}$$

$$d(\overrightarrow{u}, \overrightarrow{u}, \overrightarrow{u} - \overrightarrow{u}_\tau) - d(\overrightarrow{u}_\tau, \overrightarrow{u}_\tau, \overrightarrow{u} - \overrightarrow{u}_\tau) \le \beta_3|\overrightarrow{u} - \overrightarrow{u}_\tau|_1\|\overrightarrow{u} - \overrightarrow{u}_\tau\|_{0,\Omega}, \tag{33}$$

where β_2, β_3 are positive constants and, by considering the constant $\beta_4 = max\{\beta_2, \beta_3\}$, we have

$$\begin{aligned}
\frac{1}{2}\frac{d}{dt}\|\overrightarrow{u} - \overrightarrow{u}_\tau\|^2_{L^2(\Omega)} + \nu\|\nabla(\overrightarrow{u} - \overrightarrow{u}_\tau)\|^2_{L^2(\Omega)} \le \; &\frac{1}{\nu}\|\overrightarrow{f} - \Pi_\tau \overrightarrow{f}\|^2_{H^{-1}} + \frac{\nu}{4}|\overrightarrow{u} - \overrightarrow{u}_\tau|^2_1 + \frac{3\nu}{16}|\overrightarrow{u} - \overrightarrow{u}_\tau|^2_{1,\Omega} \\
&+ 4\nu|\overrightarrow{u}^n - \overrightarrow{u}_\tau|^2_{1,\Omega} + \frac{4\beta_4}{\nu}|\overrightarrow{u}^n - \overrightarrow{u}_\tau|^2_{1,\Omega} \qquad (34) \\
&+ \frac{4\beta_4}{\nu}\|\overrightarrow{u} - \overrightarrow{u}_\tau\|^2_{0,\Omega} + \beta_4|\overrightarrow{u}^n - \overrightarrow{u}_\tau|^2_{1,\Omega} + \beta_4\|\overrightarrow{u} - \overrightarrow{u}_\tau\|^2_{0,\Omega}.
\end{aligned}$$

We have the following inequality (for more details about this passage, we can see this paper [14]):

$$\int_{t_{m-1}}^{t_m} \|\nabla(\overrightarrow{u}^m - \overrightarrow{u}_\tau)(\cdot, x)\|^2_{0,\Omega} dx \le \frac{3}{\nu}(\eta^m)^2 + 6\int_{t_{m-1}}^{t_m} \|\nabla(\overrightarrow{u}_\tau - \overrightarrow{u}_{h\tau})(\cdot, x)\|^2_{0,\Omega} dx. \tag{35}$$

Then,

$$\begin{aligned}
\|(\overrightarrow{u} - \overrightarrow{u}_\tau)(t_m)\|^2_{L^2(\Omega)} + \nu\int_{t_{m-1}}^{t_m} \|\nabla(\overrightarrow{u} - \overrightarrow{u}_\tau)\|^2_{L^2(\Omega)} dt \quad \le \quad &\beta_5(\eta^m)^2 + \|(\overrightarrow{u} - \overrightarrow{u}_\tau)(t_{m-1})\|^2_{0,\Omega} \\
&+ \beta_6\int_{t_{m-1}}^{t_m} \|\overrightarrow{u} - \overrightarrow{u}_\tau\|^2_{0,\Omega} dt \\
&+ 6\beta_5\nu\int_{t_{m-1}}^{t_m} \|\nabla(\overrightarrow{u}_\tau - \overrightarrow{u}_{h\tau})(\cdot, x)\|^2_{L^2(\Omega)} dx \qquad (36) \\
&+ \frac{2}{\nu}\|\overrightarrow{f} - \Pi_\tau \overrightarrow{f}\|^2_{L^2(t_{m-1}, t_m; H^{-1}(\Omega))},
\end{aligned}$$

where β_5 and β_6 are two positive constants.

By utilizing inequalities (12) and (36), we can derive the desired result (28). $\square$

Theorem 3. *Under the assumptions (A_1)–(A_7), we have this estimation:*

$$\sum_{m=1}^{n}\int_{t_{m-1}}^{t_m}\|\frac{\partial}{\partial t}(\vec{u}-\vec{u}_\tau)+(\vec{u}\cdot\nabla)\vec{u}-(\vec{u}^m\cdot\nabla)\vec{u}^m+\nabla(p-\Pi_\tau\, p_\tau)\|^2_{H^{-1}(\Omega)}dt \leq$$
$$C_1\left(\sum_{m=1}^{n}\nu(\eta^m)^2+\sum_{m=1}^{n}\int_{t_{m-1}}^{t_m}\nu^2\|\vec{u}_\tau-\vec{u}_{h\tau}\|_1^2+\|\vec{f}-\Pi_\tau\vec{f}\|^2_{H^{-1}(\Omega)}dt\right), \tag{37}$$

for all $n=1,\cdots,N$, where the positive constant C_1 depends on ν, $\vec{f}$, and Ω.

Proof. By employing the results of (29) and (30), we infer

$$\begin{aligned}\|\frac{\partial}{\partial t}(\vec{u}-\vec{u}_\tau) \quad + \quad & (\vec{u}\cdot\nabla)\vec{u}-(\vec{u}^m\cdot\nabla)\vec{u}^m+\nabla(p-\Pi_\tau p_\tau)\|_{-1}\\ = \quad & \sup_{\vec{v}\in H_0^1(\Omega)}\frac{(\vec{f}-\Pi_\tau\vec{f},\vec{v})-a(\vec{u}-\vec{u}^m,\vec{v})}{\|\nabla\vec{v}\|_{L^2(\Omega)}}\\ & \leq \|\vec{f}-\Pi_\tau\vec{f}\|_{H^{-1}(\Omega)}+\nu|\vec{u}-\vec{u}_\tau|_1+\nu|\vec{u}_\tau-\vec{u}^m|_1.\end{aligned} \tag{38}$$

The result now follows by collecting estimates (28) and (35). $\square$

We consider these assumptions:

(A_8) We consider $Q^0_{n,h}\subset Q_{n,h}$ and $Q^1_{n,h}\subset Q_{n,h}$, where the spaces $Q^0_{n,h}$, $Q^1_{n,h}$ are defined by

$$Q^0_{n,h}=\{q_h\in L^2_0(\Omega);q_h|_K\in P_0(K),\ for\ all\ K\in\tau_{n,h}\}, \tag{39}$$

$$Q^1_{n,h}=\{q_h\in H^1(\Omega)\cap L^2_0(\Omega);q_h|_K\in P_1(K),\ for\ all\ K\in\tau_{n,h}\}. \tag{40}$$

(A_9) For all $1\leq p\leq N$, there exists a conforming triangulation $\widetilde{\tau}_{p;h}$, such that each element K of $\tau_{p-1;h}$ or of $\tau_{p;h}$ is the union of elements $\widetilde{K}$ of $\widetilde{\tau}_{p;h}$, such that $h_K\sim h_{\widetilde{K}}$.

Lemma 1. *Let π: $V\mapsto V$ and the operator $\pi\vec{v}=\vec{w}$, $\forall\vec{v}\in V$, where $(\vec{w},r)\in V\times Q$ is the unique solution of the Stokes problem:*

$$\begin{cases}-\triangle\vec{w}+\bigtriangledown r=0 & in\quad\Omega,\\ \nabla\cdot\vec{w}=\nabla\cdot\vec{v} & in\quad\Omega,\\ \vec{w}=\vec{0} & in\quad\partial\Omega.\end{cases} \tag{41}$$

Then, we have

(i) $\quad\pi\vec{v}=\vec{0}\ \forall\vec{v}\in Y.$

(ii) $\quad|\vec{v}-\pi\vec{v}|_1\leq|\vec{v}|_1$, $|\pi\vec{v}|_1\leq\frac{1}{\lambda}|div\,\vec{v}|_{L^2(\Omega)}$, $\forall\vec{v}\in V$, *where*

$$\lambda=\inf_{q\in Q}\sup_{\vec{v}\in V}\frac{b(\vec{v},q)}{|\vec{v}|_1|q|_0}.$$

(iii) *We suppose that assumption (A_4) holds, then*

$$\|\pi\vec{v}_h\|_{L^2(\Omega)}\leq Ch_n^\theta\|div\,\vec{v}_h\|_{L^2(\Omega)}, \tag{42}$$

for all $\vec{v}_h\in Y_{n,h}$, $1\leq n\leq N$, where

$$\begin{cases} \theta = 1 & if\ \Omega\ is\ convex, \\ \theta = \frac{1}{2} & otherwise. \end{cases} \tag{43}$$

Proof. See [14]. □

Let us consider $\overrightarrow{u}_{h\tau}$ associated with the solution $(\overrightarrow{u}_h^n)_{0\leq n\leq N}$ of system (11).

Theorem 4. *Under the assumptions (A_1)–(A_9), we have the following estimates:*

$$[[\overrightarrow{u}_\tau - \overrightarrow{u}_{h\tau}]](t_n) \leq C_2\left(\sum_{m=1}^{n} \Delta t_m \sum_{K\in\tau_{mh}} \left((1+\xi_{h\tau})(\eta_K^m)^2 + \frac{h_K^2}{\nu}\|\overrightarrow{f}^m - \overrightarrow{f}_h^m\|_{0,K}^2\right)\right)^{\frac{1}{2}} + C_3\|\overrightarrow{u}_0 - \pi_h\overrightarrow{u}_0\|_{0,\Omega}, \tag{44}$$

for all $n = 1, \cdots, N$, where the constants C_2 and C_3 are positive constants depending on ν and $\overrightarrow{f}$.

The term $\xi_{h\tau}$ is defined by

$$\xi_{h\tau} = \sup_{1\leq n\leq N} \frac{\sup_{K\in\tau_{n,h}} h_K^{2\theta_K}}{\nu\Delta t_n},$$

where

$$\begin{cases} \theta_K = 1 & if\ K\cap\partial\Omega \neq \emptyset, \\ \theta_K = \frac{1}{2} & otherwise. \end{cases} \tag{45}$$

Proof. Combining system (8) with system (15), we obtain

$$\begin{aligned}
\left(\frac{(\overrightarrow{u}^n - \overrightarrow{u}_h^n) - (\overrightarrow{u}^{n-1} - \overrightarrow{u}_h^{n-1})}{\Delta t_n}, \overrightarrow{v}\right) & + a(\overrightarrow{u}^n - \overrightarrow{u}_h^n, \overrightarrow{v}) - b(\overrightarrow{v}, p^n - p_h^n) + d(\overrightarrow{u}^n - \overrightarrow{u}_h^n, \overrightarrow{u}^n - \overrightarrow{u}_h^n, \overrightarrow{v}) \\
& = [(\overrightarrow{f}_h^n - \frac{\overrightarrow{u}_h^n - \overrightarrow{u}_h^{n-1}}{\Delta t_n} - (\overrightarrow{u}_h^n\cdot\nabla)\overrightarrow{u}_h^n, \overrightarrow{v} - \overrightarrow{v}_h) - a(\overrightarrow{u}_h^n, \overrightarrow{v} - \overrightarrow{v}_h) \\
& \quad + b(\overrightarrow{v} - \overrightarrow{v}_h, p_h^n)] + [(\overrightarrow{f}^n - \overrightarrow{f}_h^n, \overrightarrow{v} - \overrightarrow{v}_h)] \\
& \quad + [-d(\overrightarrow{u}^n - \overrightarrow{u}_h^n, \overrightarrow{u}_h^n, \overrightarrow{v}) + d(\overrightarrow{u}_h^n, \overrightarrow{u}^n - \overrightarrow{u}_h^n, \overrightarrow{v})] \\
& = F_1 + F_2 + F_3.
\end{aligned}$$

Let $\overrightarrow{e}^n = \overrightarrow{u}^n - \overrightarrow{u}_h^n$, $\overrightarrow{v} = \overrightarrow{e}^n - \pi\overrightarrow{e}^n$, and $\overrightarrow{v}_n = R_{nh}(\overrightarrow{e}^n - \pi\overrightarrow{e}^n)$. We have $\mathrm{div}(\overrightarrow{e}^n - \pi\overrightarrow{e}^n) = 0$, where R_{nh} is a Clement regularization operator [27]. We obtain

$$\begin{aligned}
(\overrightarrow{e}^n - \overrightarrow{e}^{n-1}, \overrightarrow{e}^n) + \Delta t_n\nu(\nabla\overrightarrow{e}^n, \nabla\overrightarrow{e}^n) & + \Delta t_n d(\overrightarrow{e}^n, \overrightarrow{e}^n, \overrightarrow{e}^n) = (\overrightarrow{e}^n - \overrightarrow{e}^{n-1}, \pi\overrightarrow{e}^n) \\
& + \Delta t_n\left(\nu(\nabla\overrightarrow{e}^n, \nabla\pi\overrightarrow{e}^n) + d(\overrightarrow{e}^n, \overrightarrow{e}^n, \pi\overrightarrow{e}^n) + \sum_{i=1}^{3} F_i\right).
\end{aligned} \tag{46}$$

From equality (46), Lemma 1, and by using $\pi\overrightarrow{e}^n = -\pi\overrightarrow{u}_h^n$, we obtain these inequalities:

$$\begin{aligned}
(\overrightarrow{e}^n - \overrightarrow{e}^{n-1}, \pi\overrightarrow{e}^n) & \leq \frac{1}{2}\|\overrightarrow{e}^n - \overrightarrow{e}^{n-1}\|_{L^2(\Omega)}^2 + C\xi_{h\tau}\,\nu\Delta t_h\|\mathrm{div}\,\overrightarrow{u}_h^n\|_{L^2(\Omega)}^2, \\
\nu\Delta t_n(\nabla\overrightarrow{e}^n, \nabla\pi\overrightarrow{e}^n) & \leq \frac{\nu\Delta t_n}{4}\|\nabla\overrightarrow{e}^n\|_{L^2(\Omega)}^2 + \frac{\nu\Delta t_n}{\lambda^2}\|\mathrm{div}\,\overrightarrow{u}_h^n\|_{L^2(\Omega)}^2, \\
d(\overrightarrow{e}^n, \overrightarrow{e}^n, \pi\overrightarrow{e}^n) + F_3 & \leq \frac{\nu}{8}|\overrightarrow{e}^n|_1^2 + C_4\|\mathrm{div}\,\overrightarrow{u}_h^n\|_{0,\Omega}^2 + C_5|\overrightarrow{e}^n|_{0,\Omega}^2.
\end{aligned}$$

Now, we can raise the different terms F_i, $i = 1, 2, 3$. For the first term, we have

$$
\begin{aligned}
F_1 \leq\ & C\Delta t_n\left(\sum_{K\in\tau_{n,h}}(h_K\|\vec{f}_h^n-\frac{\vec{u}_h^n-\vec{u}_h^{n-1}}{\Delta t_n}-(\vec{u}_h^n\cdot\nabla)\vec{u}_h^n+\nu\Delta\vec{u}_h^n-\nabla p_h^n\|_{L^2(K)})\right)\\
&+\sum_{E\in\varepsilon(K)}h_E^{\frac{1}{2}}\|[[\nu\partial_{n_E}\vec{u}_h^n-p_h^n\vec{n}_E]]_E\|_{L^2(E)}|\vec{v}|_1.
\end{aligned}
\quad (47)
$$

For the second, we have

$$
F_2 = (\vec{f}^n-\vec{f}_h^n,\vec{v}-\vec{v}_h)\leq C\sum_{K\in\tau_{n,h}}h_K\|\vec{f}^n-\vec{f}_h^n\|_{L^2(K)}|\vec{v}|_1. \quad (48)
$$

Using (46), we obtain

$$
\begin{aligned}
\frac{1}{2}\|\vec{e}^n\|_0^2-\frac{1}{2}\|\vec{e}^{n-1}\|_0^2 + \frac{1}{2}\nu\Delta t_n|\vec{e}^n|_1^2 \leq\ & C_4\{\sum_{K\in\tau_{n,h}}\left((\eta_K^n)^2+\frac{h_K^2}{\nu}\|\vec{f}^n-\vec{f}_h^n\|_{0,K}^2\right)\\
&+\sum_{K\in\tau_{n,h}}\left(\xi_{h\tau}\nu\Delta t_n+\frac{\nu\Delta t_n}{\lambda^2}+(\Delta t_n)^2\xi_{h\tau}\right)\|\mathrm{div}\,\vec{u}_h^n\|_{0,K}^2+\Delta t_n\|\vec{e}^n\|_0^2\}.
\end{aligned}
\quad (49)
$$

Using (49) and the discrete Gronwall lemma in [28], we obtain the result. □

Proposition 1. *According to the conditions used in Theorem 4, we have the following estimation:*

$$
\begin{aligned}
&\left(\sum_{m=1}^{n}\int_{t_{m-1}}^{t_m}\|\frac{\partial}{\partial_t}(\vec{u}_\tau-\vec{u}_{h\tau})+(\vec{u}^m\cdot\nabla)\vec{u}^m-(\vec{u}_h^m\cdot\nabla)\vec{u}_h^m+\nabla\,\Pi_\tau(p_\tau-p_{h\tau})\|_{H^{-1}(\Omega)}^2dx\right)^{\frac{1}{2}}\leq\\
&C_5\left(\sum_{m=1}^{n}\Delta t_m\sum_{K\in\tau_{m,h}}(\nu(1+\xi_{h\tau})(\eta_K^m)^2+h_K^2\|\vec{f}^m-\vec{f}_h^m\|_{0,K}^2)\right)^{\frac{1}{2}}+C_6\nu^{\frac{1}{2}}\|\vec{u}_0-\pi_h\vec{u}_0\|_{L^2(\Omega)}^2,
\end{aligned}
$$

for all $n = 1,\cdots,N$.

Proof. We can see this paper for more details [28]. □

The next step is to bound the lower bound. To achieve this, we use the results obtained previously and the standard results from [13]. As a result, we can establish the following estimation.

Theorem 5. *Under assumption (A_9) and this condition, $\exists k$, $\forall n\in[1,N]$, $\forall K\in\tau_{n;h}$, $\forall H\in V_{n,h}\cup Q_{n;h}$, $H_{|K}\in P_k$, we have this estimation:*

$$
\begin{aligned}
\eta_K^n \leq\ & C_7\Bigg(\sqrt{\nu}\,\|\nabla(\vec{u}^n-\vec{u}_h^n)\|_{0,\varpi_K}+\nu^{-\frac{1}{2}}\|\frac{(\vec{u}^n-\vec{u}_h^n)-(\vec{u}^{n-1}-\vec{u}_h^{n-1})}{\Delta t_n}+\nabla(p^n-p_h^n)\\
&+(\vec{u}^n\cdot\nabla)\vec{u}^n-(\vec{u}_h^n\cdot\nabla)\vec{u}_h^n\|_{H^{-1}(\varpi_K)}+\sqrt{\nu}\,h_K\|\vec{f}^n-\vec{f}_h^n\|_{0,\varpi_K}\Bigg),
\end{aligned}
\quad (50)
$$

for all $n = 1,\cdots,N$, where ϖ_K denotes the union of elements of $\tau_{n;h}$ that share at least a vertex with K. Moreover, we have

$$
\begin{aligned}
\eta^n \leq\ & \sqrt{\nu}\|\nabla(\vec{u}-\vec{u}_\tau)\|_{L^2(t_{n-1},t_n;L^2(\Omega))}+\nu^{-\frac{1}{2}}\|\frac{\partial}{\partial t}(\vec{u}-\vec{u}_\tau)+(\vec{u}\cdot\nabla)\vec{u}-(\vec{u}^n\cdot\nabla)\vec{u}^n+\nabla(p-\Pi_\tau p_\tau)\|_{L^2(t_{n-1},t_n;H^{-1}(\Omega))}\\
&+\nu^{-\frac{1}{2}}\|\vec{f}-\Pi_\tau\vec{f}\|_{L^2(t_{n-1},t_n,H^{-1}(\Omega))}+\sqrt{\frac{\Delta t_n}{3}\nu}\left(\|\nabla(\vec{u}^n-\vec{u}_h^n)\|_{L^2(\Omega)}+\|\nabla(\vec{u}^{n-1}-\vec{u}_h^{n-1})\|_{L^2(\Omega)}\right).
\end{aligned}
\quad (51)
$$

Proof. This result is a direct consequence of all the previous results presented in the previous theorem by summarizing all the estimations proved earlier. □

Now, we establish the equivalence between the full error $\varepsilon(t_n)$ defined by

$$\begin{aligned}\varepsilon^2(t_n) \quad = \quad & [\overrightarrow{u} - \overrightarrow{u}_\tau]^2(t_n) + [\overrightarrow{u}_\tau - \overrightarrow{u}_{h\tau}]^2(t_n) + \frac{1}{\nu}\sum_{m=1}^{n}\int_{t_{m-1}}^{t_m} \| \frac{\partial}{\partial t}(\overrightarrow{u} - \overrightarrow{u}_\tau) + \nabla(p - \Pi_\tau\, p_\tau) \\ & + (\overrightarrow{u}\cdot\nabla)\overrightarrow{u} - (\overrightarrow{u}^m\cdot\nabla)\overrightarrow{u}^m\|^2_{H^{-1}(\Omega)}dx + \frac{1}{\nu}\sum_{m=1}^{n}\int_{t_{m-1}}^{t_m}\|\frac{(\overrightarrow{u}^m - \overrightarrow{u}_h^m) - (\overrightarrow{u}^{m-1} - \overrightarrow{u}_h^{m-1})}{\triangle t_m} \\ & + \nabla\,\Pi_\tau(p_\tau - p_{h\tau}) + (\overrightarrow{u}^m\cdot\nabla)\overrightarrow{u}^m - (\overrightarrow{u}_h^m\cdot\nabla)\overrightarrow{u}_h^m\|^2_{H^{-1}(\Omega)}dx,\end{aligned} \tag{52}$$

for all $n = 1, \cdots, N$ and the a posteriori error η_S defined by

$$\eta_S = \left[\sum_{m=1}^{n}\left((\eta^m)^2 + \triangle t_m \sum_{K\in\tau_{m,h}}(\eta_K^m)^2\right)\right]^{\frac{1}{2}}. \tag{53}$$

By summarizing and incorporating the previous results, we can conclude this theorem.

Theorem 6. *Under the assumptions (A_1)–(A_9), we have*

$$m_1\,\eta_S \le \varepsilon(t_n) \le M_2\,\eta_S, \tag{54}$$

where m_1 and M_2 are positive constants.

Proof. This result directly follows from all the previous results presented in the previous theorem. It is a summary of all the estimations that have been proven earlier, leading to this particular estimation. □

5. Numerical Simulation

In this section, we will present the results of two numerical simulations using the Finite Element Method. The main objective is to assess the performance of our method and analyze the obtained results in two dimensions:

- In the first test, we compared the numerical results obtained using Matlab code with those obtained from the commercial software ADINA system. The simulations are conducted in a rectangular L-shaped domain, and we will evaluate the accuracy and reliability of our method by comparing the results with ADINA. ADINA, short for "Automatic Dynamic Incremental Nonlinear Analysis," is a comprehensive finite element analysis software package widely acclaimed for its versatility in tackling complex problems across various domains, including engineering and computational mechanics. This powerful tool has gained recognition for its proficiency, particularly in scenarios involving heat and fluid flow analysis, such as in the case of the "Cooling of an Electronic Component." ADINA excels in simulating and predicting the behavior of thermal and fluid systems under diverse conditions. It leverages advanced numerical methods to precisely model heat transfer phenomena, encompassing conduction, convection, and radiation, as well as fluid flow dynamics, spanning from laminar to turbulent flows.
- In the second test, we focused on simulating the time-dependent flow past a cylinder using COMSOL Multiphysics. We varied the values of the parameter β in the boundary condition to investigate its effects on the flow behavior.

By conducting these numerical simulations and analyzing the obtained results, we aim to validate the accuracy and effectiveness of our Finite Element Method for a nonlinear differential equation with a general boundary condition.

5.1. Test 1 (L-Shaped Domain)

In the first test, we conducted a numerical simulation of the NS problem (1) with a focus on comparing the results obtained using the Finite Element Method. The comparison involved assessing the performance of the Matlab code against the results obtained from the ADINA system. The simulation revolved around studying the flow within a rectangular L-shaped duct with a sudden expansion. The inflow boundary, located at $x = -1$, extended along the y-direction within the range $0 \leq y \leq 1$ and was subjected to a Poiseuille flow profile. The duct walls were characterized by a no-flow condition, resulting in zero velocity along the walls. At the outflow boundary, positioned at $x = 5$ with $-1 < y < 1$, we applied the Neumann condition (55) to simplify the comparison:

$$\begin{cases} \nu \frac{\partial u_x}{\partial x} - p & = 0, \\ \frac{\partial u_y}{\partial x} & = 0, \end{cases} \tag{55}$$

ensuring the mean outflow pressure was automatically set to zero.

The figures in this section offer visual representations of the computed results for the flow in our domain. Streamlined plots illustrate the flow lines within the domain, providing a visual depiction of the fluid's path and direction. Additionally, velocity vector plots showcase the magnitude and direction of the velocity field through vectors, enabling comprehensive visualization of the flow characteristics, including areas of high and low velocity. These visual representations serve as valuable tools for understanding and interpreting the computed results of the flow in the domain. They provide insights into the overall flow behavior, patterns, and variations, facilitating the analysis and interpretation of the numerical simulation.

We set the final time for this test as $T = 100$, employing a 32×96 square grid with a $Q_1 - Q_0$ approximation to discretize the problem. The numerical simulation took into account a viscosity value of $\nu = 1/600$ to analyze the fluid flow behavior. The computed streamlines for the Matlab Code and ADINA system are presented in Figures 1 and 2, respectively.

Figure 1 presents the streamlines obtained using the Matlab code.

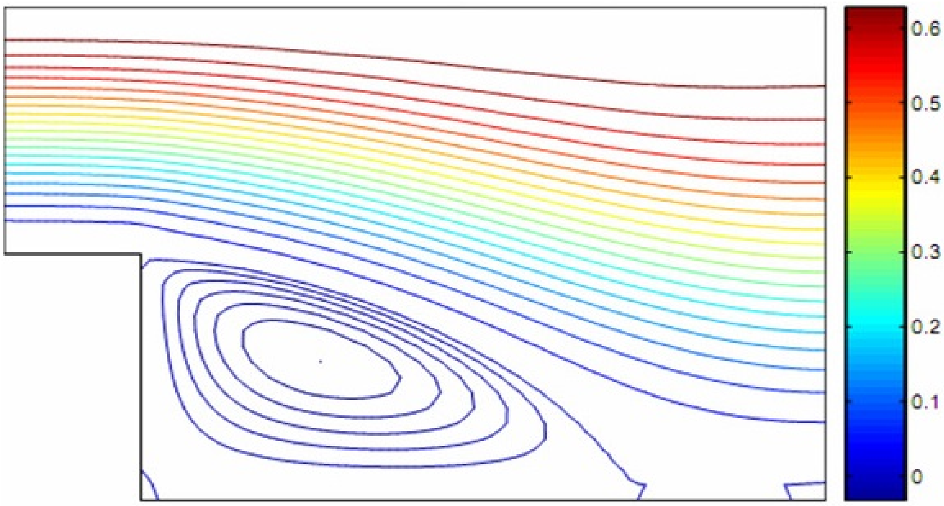

Figure 1. Streamlined with Matlab code.

Figure 2 presents the streamlines obtained using the ADINA system.

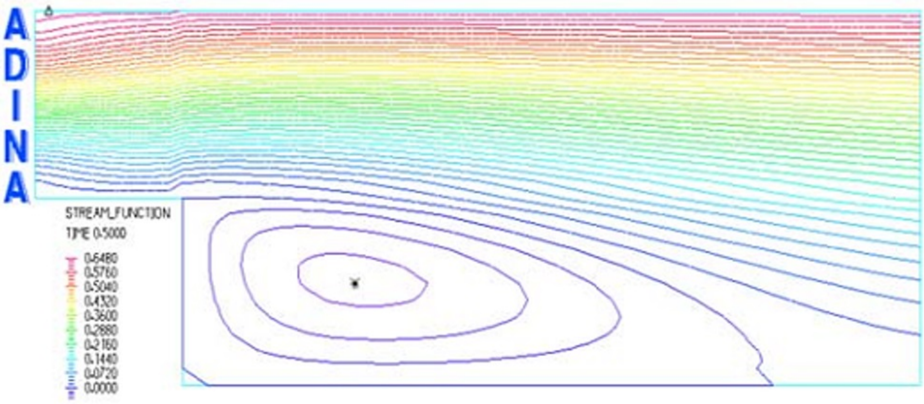

Figure 2. Streamlined with ADINA system.

The flow development revealed the formation of a single recirculation zone downstream of the step. Notably, a close examination of the results depicted in Figures 1 and 2 demonstrated a high degree of similarity or strong correlation between them.

In Figures 1 and 2, we present the vorticity contours for the flow analysis using the Matlab Code and ADINA system, respectively. In Figure 3, we showcase the vorticity contours obtained from the Matlab code.

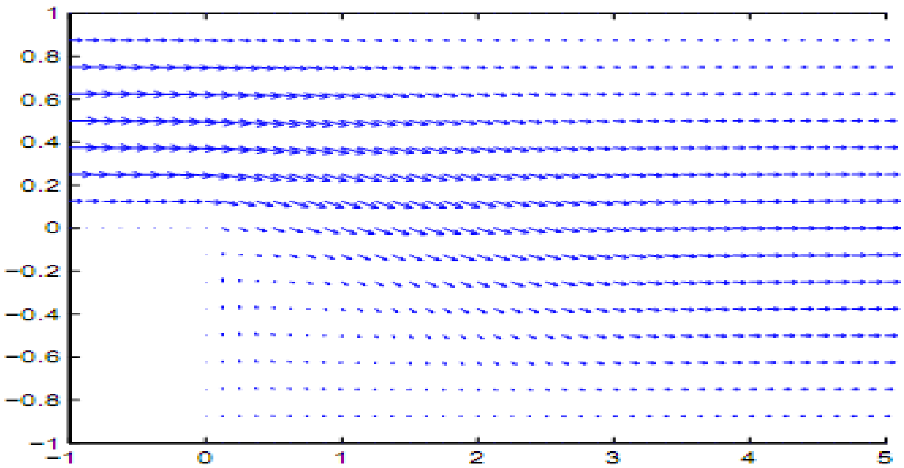

Figure 3. Vorticity contours with Matlab code.

In Figure 4, we present the solution obtained using the ADINA system.

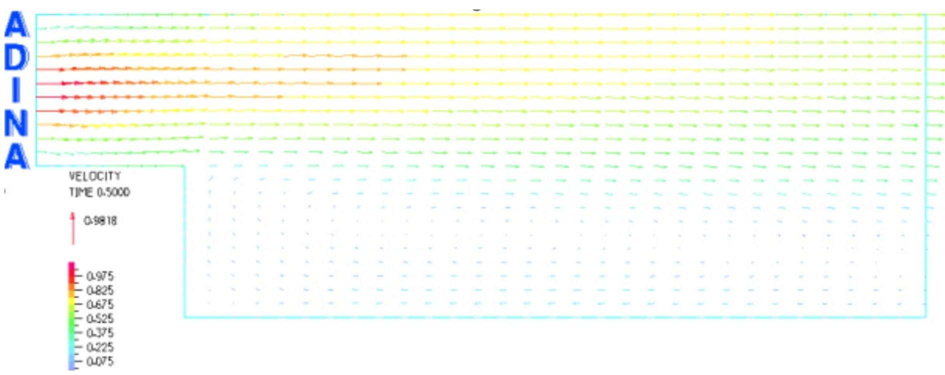

Figure 4. Vorticity contours with the ADINA system.

This visual comparison suggests that both the Matlab Code and the ADINA system yield consistent and comparable results for the fluid flow analysis within the rectangular *L*-shaped duct with a sudden expansion.

Figure 5 depicts the pressure solutions at $T = 120$ for different viscosity values: $\nu = 1$, $\nu = 1/40$, $\nu = 1/100$, and $\nu = 1/500$. The numerical simulations were conducted using a 32×96 square grid and the $Q_1 - P_0$ approximation scheme.

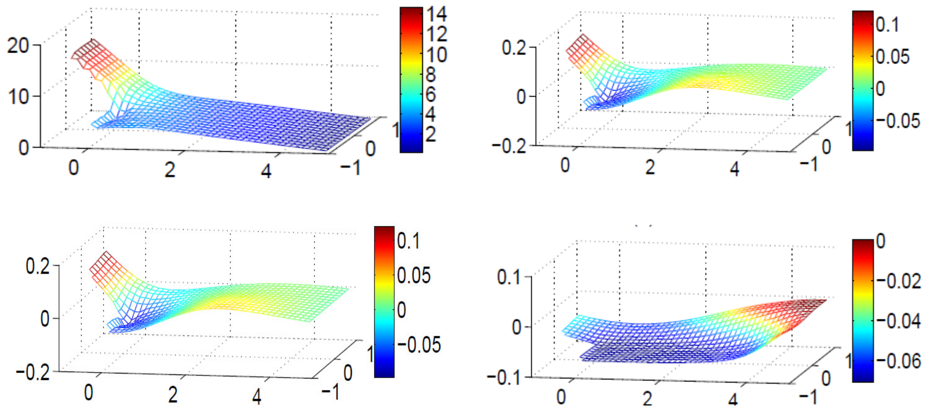

Figure 5. Pressure for the viscosity value $\nu = 1$ (left at the top), $\nu = 1/40$ (right at the top), $\nu = 1/100$ (left at the down), and $\nu = 1/500$ (right at the down).

We can observe the evolution of the pressure by changing the value of μ specified in the boundary condition. Now, with $\nu = 1/600$ fixed, we consistently used the stabilized $Q_1 - P_0$ method and, in Figure 6, we observed the pressure distributions at specific time steps: $t = 10.25$, $t = 50.15$, $t = 100.33$, and $t = 450.02$.

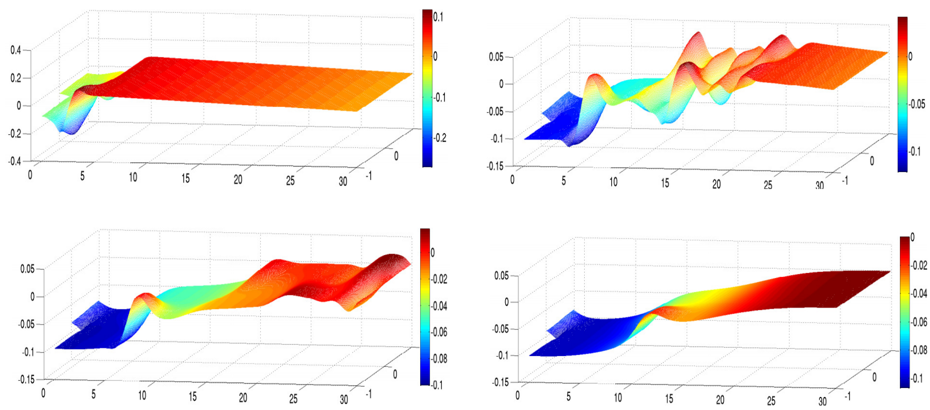

Figure 6. Pressure at $t = 10.25$ (left at the top), $t = 50.15$ (right at the top), $t = 100.33$ (left at the down), and $t = 450.02$ (right at the down).

At early times, the pressure distribution illustrated in Figure 6, shows the development of potential flow "sheets" along the rigid walls. This phenomenon is a significant and challenging aspect of impulsively-started viscous flow. The formation of these potential flow sheets is particularly relevant for understanding and modeling the dynamics of the fluid flow in this scenario. A more comprehensive and detailed discussion of this feature can be found in Section 3.19 in this paper [29].

Table 1 provides the number of preconditioned GMRES iterations at time $T = 190$ for different values of β in the $Q_1 - P_0$ element. We compared these results with those obtained using the $Q_2 - P_1$ element.

Table 1. Number of preconditioned GMRES iterations at $T = 190$.

FEM Method	Coarse Mesh		Fine Mesh	
	Standard	**Rescaled**	**Standard**	**Rescaled**
$Q_2 - P_1$	14	12	10	9
$Q_1 - P_0$ with $\alpha = 0$	7	7	7	7
$Q_1 - P_0$ with $\alpha = 1/4\nu$	7	10	8	9
$Q_1 - P_0$ with $\alpha = 1/4$	34	82	32	68

The comparison presented in Table 1 underscores the advantages of using the optimally stabilized system with $\alpha = 1/4\nu$. This approach demonstrates superior conditioning, leading to a reduced number of GMRES iterations for convergence. The reduced number of iterations signifies more efficient and faster solution convergence, which is highly beneficial for computational efficiency and reduced computational time. Indeed, the results presented in this simulation demonstrate the performance and effectiveness of the proposed numerical approach for studying the time-dependent Navier–Stokes equations.

To estimate the error and provide information about the accuracy and quality of the numerical solution, we present a comparison between the uniform and adaptive methods in Figure 7. The figure visually illustrates and compares the performance or results obtained by each method, offering a graphical representation of their respective outcomes.

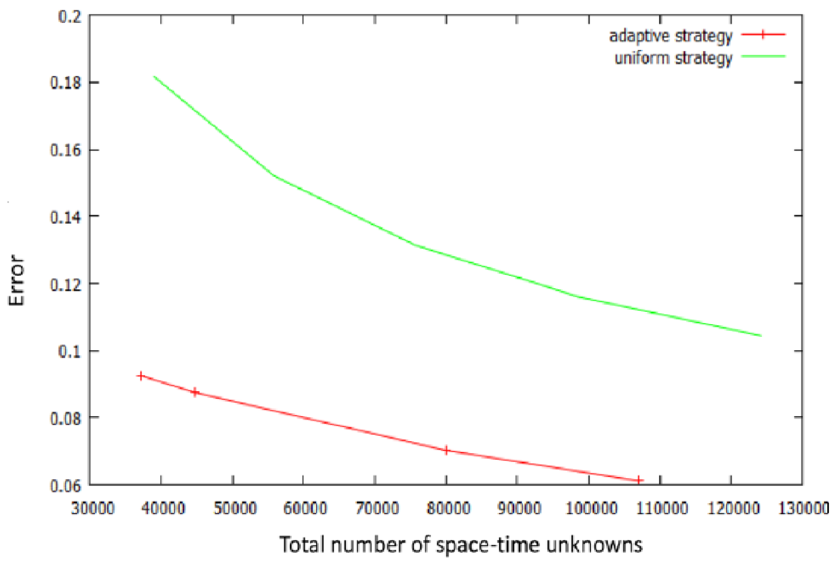

Figure 7. Comparison of the errors obtained with the uniform and adaptive methods.

By observing the results, it becomes apparent that both the error and the estimated error tend to converge to zero as the time steps become increasingly smaller. This observation suggests that taking smaller time steps can effectively reduce both the error and the estimated error in the numerical solution. Decreasing the time step size highlights the significance of selecting appropriate time steps to ensure accurate and reliable numerical solutions.

5.2. Test 2 (Flow Past a Cylinder)

The model presented in this simulation investigates the unsteady incompressible flow around a long cylinder positioned in a channel at a right angle to the incoming fluid. The asymmetrical placement of the cylinder in the flow creates an unstable flow pattern, and the simulation aims to study the development of periodic flow behavior. The appearance of this periodic flow pattern is challenging to predict and is influenced by various factors, with the Reynolds number being a key predictor. In this simulation, the Reynolds number is set to 100, leading to the formation of a developed Karman vortex street, providing valuable insights into the transition process in unsteady flows. The investigation of such flows is essential in various engineering and fluid mechanics applications, offering a deeper understanding of flow phenomena and their influence on the behavior of bodies immersed in fluids.

This model is carried out using the Navier–Stokes Equation (1). Specifically, we are interested in comparing the results obtained by varying the values of the parameter β (β: $\beta = 10^4$, $\beta = 1$, $\beta = 10^{-2}$, and $\beta = 0$) in the boundary condition (2), and we conducted numerical tests with and without a posterior error estimation by using an a posteriori estimator. These values of β represent different scenarios of boundary conditions, allowing us to explore the impact of this parameter on the flow characteristics around the cylinder. To assess the performance of this study, we compared the results with those obtained using fine meshes.

To carry out the simulation, we chose a final time of $T = 7$ s and divided the time steps into two intervals: $\Delta t = 0.2$ s for the time interval [0, 3.4] and $\Delta t = 0.02$ s for the time interval [3.5, 7]. This time discretization allowed us to capture the time-dependent behavior of the flow accurately; we chose three instances of $t = 2$ s, $t = 4$ s, and $t = 7$ s. Figure 8 illustrates the domain and boundary of the problem under consideration.

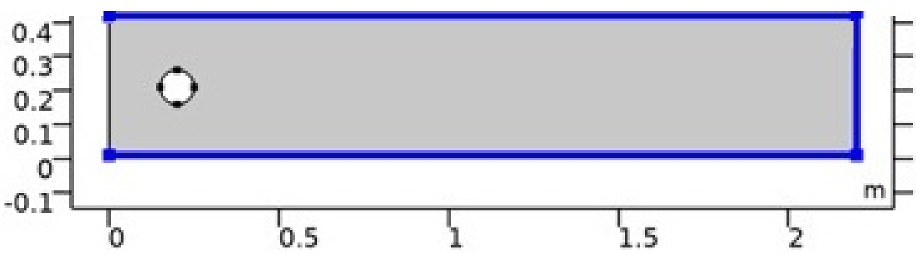

Figure 8. Domain and boundary condition for our problem "Flow Past a Cylinder".

In the blue regions, we applied the general boundary condition while, in the remaining parts, we imposed the Dirichlet boundary condition $u = f$. We took $f = 0$ on the contour of the circle and $f = U_{\text{mean}} \times \frac{6y(H-y)}{H^2} \times \text{step1}(t[\text{s}])$, where $U_{\text{mean}} = 1$ m/s and $H = 0.41$ m.

The adaptive mesh refinement (AMR) technique allowed us to dynamically adjust the mesh resolution based on the solution's accuracy, focusing computational resources where they were most needed and reducing the mesh density in less critical regions.

Figure 9 illustrates the comparison of the mesh used in the simulation with and without adaptive mesh refinement, respectively.

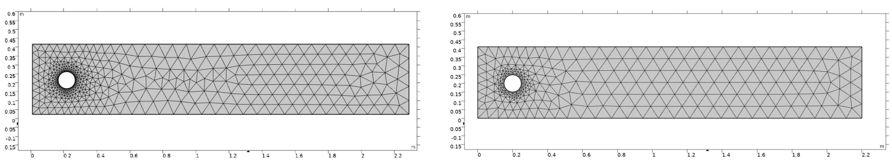

Figure 9. Comparison of the mesh used in the simulation with (**left**) and without (**right**) adaptive mesh refinement.

Table 2 provides the number of elements used in different discretizations. The table reveals that the number of elements in the very small mesh is significantly larger than in the other meshes to provide a high-resolution representation of the flow domain, resulting in a finer grid and a larger number of elements. On the other hand, the number of elements in the normal mesh and the adaptive mesh refinement are less and very close to each other.

Table 2. The number of elements for different discretizations applied in this simulation.

Types of Mesh	Number of Border Elements	Number of Exterior Elements
Fine mesh (FM)	2014	300,982
Normal mesh (NM)	116	900
Adaptive mesh refinement (AMR)	106	840

We will now proceed to approximate the velocity and pressure profiles for different cases of β ($\beta = 10^{-4}$, $\beta = 10^2$, $\beta = 1$, and $\beta = 0$) at three different instances: $t = 2$ s, $t = 4$ s, and $t = 7$ s. The Finite Element Method (FEM) will be used to approximate this model in three types of meshes (FM, NM, and AMR) for comparing the results obtained.

Now, we present the figures that illustrate the results obtained for our study and allow us to compare the results. Figures 10–12 display the velocity for $\beta = 10^{-4}$ in different meshes (FM, NM, and AMR).

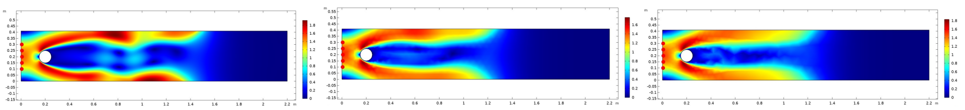

Figure 10. Velocity at $t = 2$ s in different meshes: FM (**left**), NM (**middle**), and AMR (**right**).

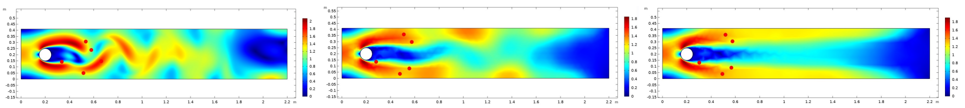

Figure 11. Velocity at $t = 4$ s in different meshes: FM (**left**), NM (**middle**), and AMR (**right**).

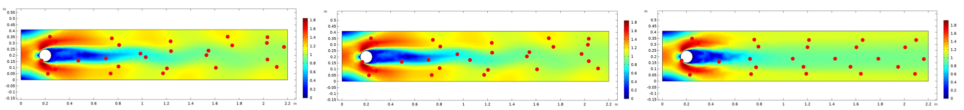

Figure 12. Velocity at $t = 7$ s in different meshes: FM (**left**), NM (**middle**), and AMR (**right**).

Figures 13–15 display the pressure profiles for $\beta = 10^{-4}$ in different meshes at different times: $t = 2$ s, $t = 4$ s, and $t = 7$ s.

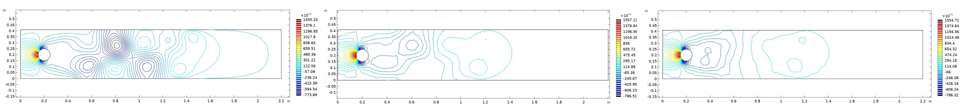

Figure 13. Pressure profiles at $t = 2$ s in different meshes: FM (**left**), NM (**middle**), and AMR (**right**).

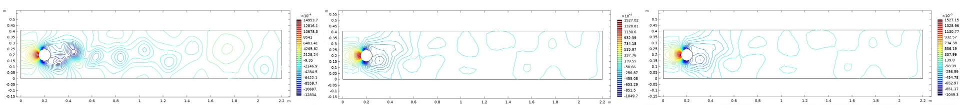

Figure 14. Pressure profiles at $t = 4$ s in different meshes: FM (**left**), NM (**middle**), and AMR (**right**).

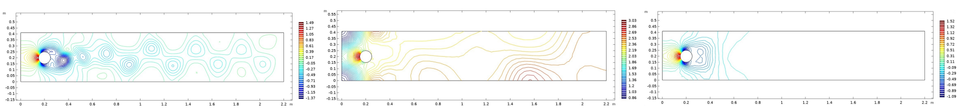

Figure 15. Pressure profiles at $t = 7$ s in different meshes: FM (**left**), NM (**middle**), and AMR (**right**).

Figures 16–18 present the velocity for $\beta = 10^2$ at different times.

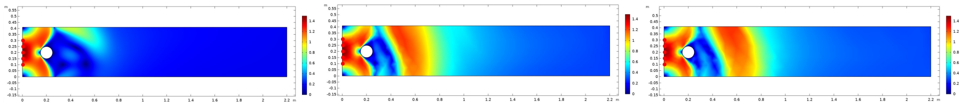

Figure 16. Velocity at $t = 2$ s in different meshes: FM (**left**), NM (**middle**), and AMR (**right**).

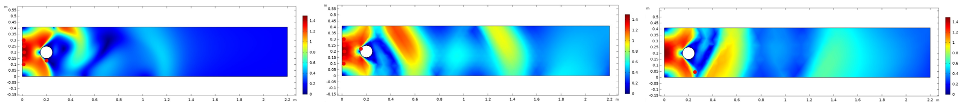

Figure 17. Velocity at $t = 4$ s in different meshes: FM (**left**), NM (**middle**), and AMR (**right**).

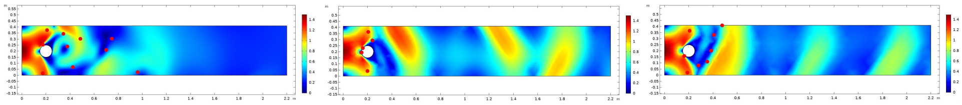

Figure 18. Velocity at $t = 7$ s in different meshes: FM (**left**), NM (**middle**), and AMR (**right**).

Figures 19–21 display the pressure profiles for $\beta = 10^2$ at different times.

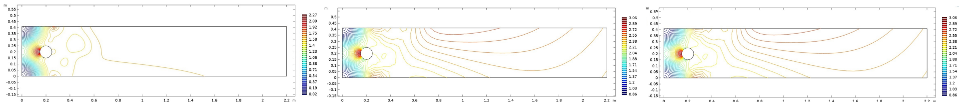

Figure 19. Pressure profiles at $t = 2$ s in different meshes: FM (**left**), NM (**middle**), and AMR (**right**).

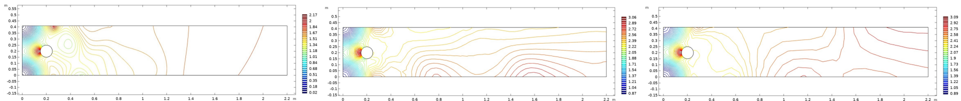

Figure 20. Pressure profiles at $t = 4$ s in different meshes: FM (**left**), NM (**middle**), and AMR (**right**).

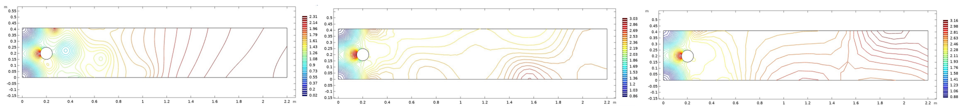

Figure 21. Pressure profiles at $t = 7$ s in different meshes: FM (**left**), NM (**middle**), and AMR (**right**).

Figures 22–24 present the velocity for $\beta = 1$ at different times.

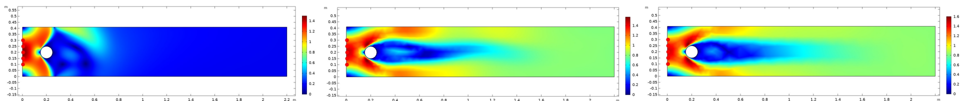

Figure 22. Velocity at $t = 2$ s in different meshes: FM (**left**), NM (**middle**), and AMR (**right**).

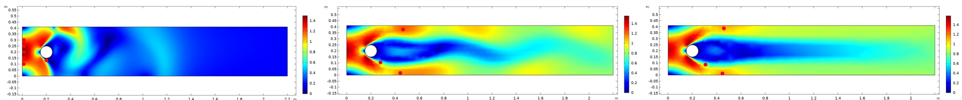

Figure 23. Velocity at $t = 4$ s in different meshes: FM (**left**), NM (**middle**), and AMR (**right**).

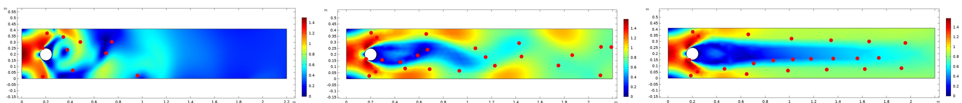

Figure 24. Velocity at $t = 7$ s in different meshes: FM (**left**), NM (**middle**), and AMR (**right**).

Figures 25–27 display the pressure profiles for $\beta = 1$ at different times.

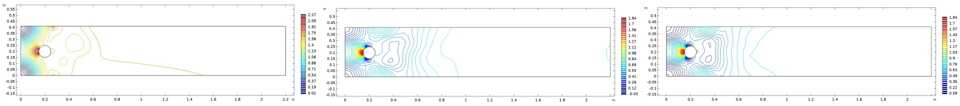

Figure 25. Pressure profiles at $t = 2$ s in different meshes: FM (**left**), NM (**middle**), and AMR (**right**).

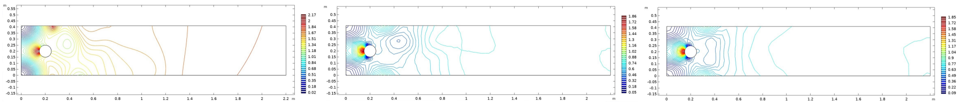

Figure 26. Pressure profiles at $t = 4$ s in different meshes: FM (**left**), NM (**middle**), and AMR (**right**).

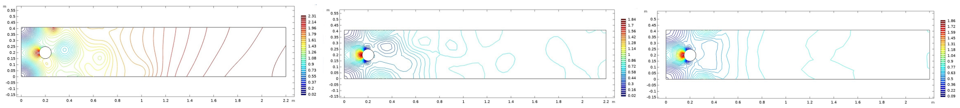

Figure 27. Pressure profiles at $t = 7$ s in different meshes: FM (**left**), NM (**middle**), and AMR (**right**).

Figures 28–30 present the velocity for $\beta = 0$ at different times.

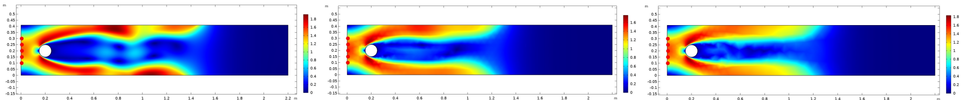

Figure 28. Velocity at $t = 2$ s in different meshes: FM (**left**), NM (**middle**), and AMR (**right**).

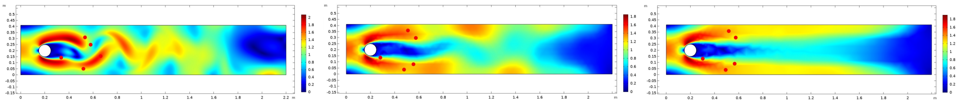

Figure 29. Velocity at $t = 4$ s in different meshes: FM (**left**), NM (**middle**), and AMR (**right**).

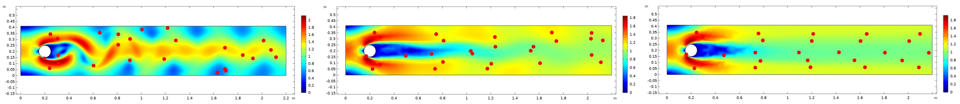

Figure 30. Velocity at $t = 7$ s in different meshes: FM (**left**), NM (**middle**), and AMR (**right**).

Figures 31–33 display the pressure profiles for $\beta = 0$ at different times.

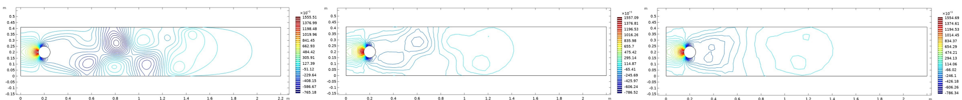

Figure 31. Pressure profiles at $t = 2$ s in different meshes: FM (**left**), NM (**middle**), and AMR (**right**).

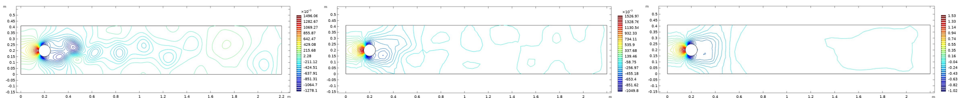

Figure 32. Pressure profiles at $t = 4$ s in different meshes: FM (**left**), NM (**middle**), and AMR (**right**).

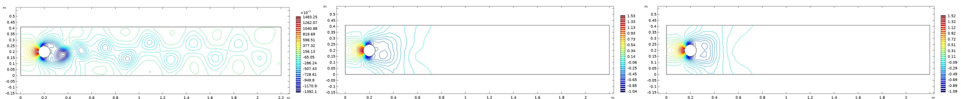

Figure 33. Pressure profiles at $t = 7$ s in different meshes: FM (**left**), NM (**middle**), and AMR (**right**).

By comparing the results of the velocity and pressure profiles presented in Figures 10–33 for different values of β in three different meshes (FM, NM, and AMR), we observed noticeable differences, especially in the regions where the general boundary condition was applied. The parameter β plays a crucial role in determining the flow behavior near the boundary and significantly influences the velocity and pressure distributions within the domain. For very small values of β, the results tend to closely resemble or approach the Dirichlet condition, indicating that the new boundary condition becomes less influential, and the flow behavior near the boundary is dominated more by the Dirichlet condition. Conversely, for larger values of β, the new boundary condition becomes more prominent, exerting a stronger influence on the flow behavior near the boundary. This is evident in the velocity and pressure profiles, which deviate more significantly from the Dirichlet condition with increasing values of β. The choice of β has a direct impact on the accuracy and reliability of the numerical solution, making it an essential parameter to consider in modeling and simulations. By comparing the results with the referential test, we can observe the results obtained by adaptive mesh refinement are more important.

In conclusion, the comparison of the results obtained using adaptive mesh refinement (AMR) and normal mesh (NM) with the fine mesh (FM) reveals that AMR yields more significant and influential results compared to NM. The adaptive mesh refinement technique provides improved accuracy and reliability, making a significant contribution to the overall outcomes compared to the nested mesh approach. One key advantage of using a posteriori error estimation for the Navier–Stokes problem is the ability to obtain accurate numerical solutions with a reduced number of elements compared to uniform meshes or traditional refinement strategies. This not only reduces computational expenses but also accelerates the simulation process, making it more efficient. By employing AMR, researchers can achieve higher-resolution solutions in regions of interest while maintaining a coarser mesh in other areas. This adaptive approach optimizes computational resources and enhances the precision of the simulation results, particularly in cases where the flow behavior exhibits varying complexities across the domain.

In the next step, we propose coupling the Navier–Stokes equation with the Darcy equation instead of the Stokes equation. By coupling the Navier–Stokes equation with the Darcy equation, we can capture the fluid flow in porous media more accurately and effectively. This coupled model is particularly relevant when studying flow phenomena that involve interactions between the fluid flow in the free domain and the flow within the porous medium. Another application of this model is for the problem of the mass-based hybridity model for thermomicropolar binary nanofluid flow defined in this paper [30].

6. Concluding Remarks

In this paper, our primary focus was on numerically solving a nonlinear partial differential equation governing the flow of incompressible fluids. Specifically, we employed the Finite Element Method (FEM) to solve the unsteady Navier–Stokes equations with a general boundary condition. We investigated a posteriori error estimates to control the error of our numerical solution. To this end, we introduced two types of error indicators: one for time discretization and another for space discretization. These error indicators allowed us to estimate the error in our numerical solution, enabling us to identify regions where the approximation might be less accurate. Furthermore, we established the equivalence between the sum of the two types of error indicators and the total error. This equivalence provided a comprehensive understanding of the overall error in our numerical solution and validated the accuracy and reliability of our approach.

To validate the proposed numerical methods, we conducted extensive numerical experiments and compared the results with findings reported in the literature, as well as results obtained from the commercial software ADINA system. These comparisons aimed to assess the accuracy and reliability of our numerical techniques. Encouragingly, we observed good agreement between our numerical results and those from the literature and ADINA, confirming that our methods were implemented correctly and produced accurate solutions. Additionally, we performed comparisons both with and without using the a posteriori error estimator, as well as with a very small mesh. These comparisons emphasized the significance of the estimator, as the results obtained with the estimator were more realistic and reliable than the other methods.

Overall, the consistent and satisfactory comparisons support the credibility of our numerical approach and demonstrate its capability to simulate fluid flow and effectively solve the unsteady Navier–Stokes equations. The use of a posteriori error estimates further enhances the accuracy and trustworthiness of our numerical solutions.

Author Contributions: Conceptualization, O.E.M. and M.L.S.; methodology, O.E.M. and S.V; software, O.E.M. and A.E.; validation, O.E.M., A.E. and N.N.; formal analysis, O.E.M.; investigation, L.E.O.; resources, S.V.; writing—original draft preparation, O.E.M. and A.E.A.; writing—review and editing, S.V.; visualization, A.E. and N.N.; supervision, O.E.M.; project administration, O.E.M. All authors have read and agreed to the published version of the manuscript.

Funding: This research received no external funding.

Data Availability Statement: Data are contained within the article.

Conflicts of Interest: The authors declare no conflict of interest.

References

1. Rao, C.; Sun, H.; Liu, Y. Physics-informed deep learning for incompressible laminar flows. *Theor. Appl. Mech. Lett.* **2020**, *10*, 207–212. [CrossRef]
2. Muldoon, F.H. *Numerical Methods for the Unsteady Incompressible Navier-Stokes Equations and Their Application to the Direct Numerical Simulation of Turbulent Flows*; Louisiana State University and Agricultural & Mechanical College: Baton Rouge, LA, USA, 2004; pp. 32–58.
3. Zhu, T.; Waluga, C.; Wohlmuth, B.; Manhart, M. A study of the time constant in unsteady porous media flow using direct numerical simulation. *Transp. Porous Media* **2014**, *104*, 161–179. [CrossRef]
4. Kim, W.; Menon, S. An unsteady incompressible Navier–Stokes solver for large eddy simulation of turbulent flows. *Int. J. Numer. Methods Fluids* **1999**, *31*, 983–1017. [CrossRef]
5. Suss, A.; Mary, I.; Le Garrec, T.; Marié, S. Comprehensive comparison between the lattice Boltzmann and Navier–Stokes methods for aerodynamic and aeroacoustic applications. *Comput. Fluids* **2023**, *257*, 105881. [CrossRef]
6. He, Y. The Euler implicit/explicit scheme for the 2*D* time-dependent Navier-Stokes equations with smooth or non-smooth initial data. *Math. Comput.* **2008**, *77*, 2097–2124. [CrossRef]
7. Bernardi, C.; Raugel, G. A conforming finite element method for the time-dependent Navier–Stokes equations. *SIAM J. Numer. Anal.* **1985**, *22*, 455–473. [CrossRef]
8. Yan, Y. Galerkin finite element methods for stochastic parabolic partial differential equations. *SIAM J. Numer. Anal.* **2005**, *43*, 1363–1384. [CrossRef]
9. He, Y. Optimal error estimate of the penalty finite element method for the time-dependent Navier-Stokes equations. *Math. Comput.* **2005**, *74*, 1201–1216. [CrossRef]
10. He, Y.; Li, K. Two-level stabilized finite element methods for the steady Navier–Stokes problem. *Computing* **2005**, *74*, 337–351. [CrossRef]
11. John, V.; Kaya, S. A finite element variational multiscale method for the Navier–Stokes equations. *SIAM J. Sci. Comput.* **2005**, *26*, 1485–1503. [CrossRef]
12. Koubaiti, O.; El-mekkaoui, J.; Elkhalfi, A. Complete study for solving Navier-Lamé equation with new boundary condition using mini element method. *Int. J. Mech.* **2018**, *12*, 46–58.
13. Verfürth, R. A posteriori error estimation and adaptive mesh-refinement techniques. *J. Comput. Appl. Math.* **1994**, *50*, 67–83. [CrossRef]
14. Bernardi, C.; Verfürth, R. A posteriori error analysis of the fully discretized time-dependent Stokes equations. *ESAIM Math. Model. Numer. Anal.* **2004**, *38*, 437–455. [CrossRef]
15. Nejat, A.; Ollivier-Gooch, C. Effect of discretization order on preconditioning and convergence of a high-order unstructured Newton-GMRES solver for the Euler equations. *J. Comput. Phys.* **2008**, *227*, 2366–2386. [CrossRef]
16. Saad, Y.; Schultz, M.H. GMRES: A generalized minimal residual algorithm for solving nonsymmetric linear systems. *SIAM J. Sci. Stat. Comput.* **1986**, *7*, 856–869. [CrossRef]
17. Ainsworth, M.; Oden, J.T. A posteriori error estimation in finite element analysis. *Comput. Methods Appl. Mech. Eng.* **1997**, *142*, 1–88. [CrossRef]
18. Temam, R. *Navier-Stokes Equations: Theory and Numerical Analysis*; American Mathematical Society: Providence, RI, USA, 2001; Volume 343.
19. Nicaise, S.; Soualem, N. *A Posteriori Error Estimates for a Nonconforming Finite Element Discretization of the Time-Dependent Stokes Problem*; Walter de Gruyter GmbH & Co. KG: Berlin, Germany, 2007.

20. Liao, Q.; Silvester, D. *Fast Implicit Solvers Using Stabilized Mixed Approximation*; Manchester Institute for Mathematical Sciences, University of Manchester: Manchester, UK, 2011.
21. Li, J.; He, Y.; Chen, Z. A new stabilized finite element method for the transient Navier–Stokes equations. *Comput. Methods Appl. Mech. Eng.* **2007**, *197*, 22–35. [CrossRef]
22. Shan, L.; Hou, Y. A fully discrete stabilized finite element method for the time-dependent Navier–Stokes equations. *Appl. Math. Comput.* **2009**, *215*, 85–99. [CrossRef]
23. Raviart, P.-A.; Thomas, J.-M. A mixed finite element method for 2nd order elliptic problems. In *Mathematical Aspects of Finite Element Methods: Proceedings of the Conference Held in Rome, 10–12 December 1975*; Springer: Berlin/Heidelberg, Germany, 2006; pp. 292–315.
24. Elman, H.C.; Silvester, D.J.; Wathen, A.J. *Finite Elements and Fast Iterative Solvers: With Applications in Incompressible Fluid Dynamics*; Oxford University Press: Oxford, UK, **2014**.
25. Elman, H.; Howle, V.E.; Shadid, J.; Silvester, D.; Tuminaro, R. Least squares preconditioners for stabilized discretizations of the Navier–Stokes equations. *SIAM J. Sci. Comput.* **2008**, *30*, 290–311. [CrossRef]
26. Gauthier, A.; Saleri, F.; Veneziani, A. A fast preconditioner for the incompressible Navier Stokes Equations. *Comput. Vis. Sci.* **2004**, *6*, 105–112. [CrossRef]
27. Clément, P. Approximation by finite element functions using local regularization. *Rev. Fr. d'Autom. Inform. Rech. Opér. Anal. Numér.* **1975**, *9*, 77–84. [CrossRef]
28. Girault, V.; Raviart, P.-A. *Finite Element Methods for Navier-Stokes Equations: Theory and Algorithms*; Springer Nature: Berlin/Heidelberg, Germany, 2012; Volume 5.
29. Gresho, P.M.; Sani, R.L. *Incompressible Flow and the Finite Element Method. Volume 1: Advection-Diffusion and Isothermal Laminar Flow*; John Wiley and Sons, Inc.: Hoboken, NJ, USA, 1998.
30. Behrouz, M.; Dinarv, S.; Yazdi, M.E.; Tamim, H.; Pop, I.; Chamkha, A.J. Mass-based hybridity model for thermomicropolar binary nanofluid flow: First derivation of angular momentum equation. *Chin. J. Phys*. **2023**, *83*, 165–184. [CrossRef]